HHS Public Access

Author manuscript

Cell Rep. Author manuscript; available in PMC 2022 October 25.

Published in final edited form as:

Cell Rep. 2022 September 20; 40(12): 111358. doi:10.1016/j.celrep.2022.111358.

A proliferative to invasive switch is mediated by srGAP1 downregulation through the activation of TGF-β2 signaling

Chandrani Mondal[1], **Majo J. Gacha-Garay**[2,10], **Kathryn A. Larkin**[2,10], **Rebecca C. Adikes**[2,10], **Julie S. Di Martino**[1], **Chen-Chi Chien**[3], **Madison Fraser**[1], **Ireti Eni-aganga**[1], **Esperanza Agullo-Pascual**[4], **Katarzyna Cialowicz**[4], **Umut Ozbek**[5], **Alexandra Naba**[6,7], **Angelo Gaitas**[3], **Tian-Ming Fu**[8], **Srigokul Upadhyayula**[9], **Eric Betzig**[8,9], **David Q. Matus**[2], **Benjamin L. Martin**[2], **Jose Javier Bravo-Cordero**[1,11,*]

[1]Department of Medicine, Division of Hematology and Oncology, The Tisch Cancer Institute, Icahn School of Medicine at Mount Sinai, New York, NY 10029, USA

[2]Biochemistry and Cell Biology Department, Stony Brook University, Stony Brook, NY 11794, USA

[3]Department of Neurology, Icahn School of Medicine at Mount Sinai, New York, NY 10029, USA

[4]Microscopy and Advanced Bioimaging Core, Icahn School of Medicine at Mount Sinai, New York, NY 10029, USA

[5]Department of Population Health Science and Policy, Icahn School of Medicine at Mount Sinai, New York, NY 10029, USA

[6]Department of Physiology & Biophysics, University of Illinois at Chicago, Chicago, IL 60612, USA

[7]University of Illinois Cancer Center, University of Illinois at Chicago, Chicago, IL 60612, USA

[8]Janelia Research Campus, Howard Hughes Medical Institute, Ashburn, VA 20147, USA

[9]Department of Molecular and Cellular Biology, UC Berkeley, CA 94720, USA

[10]These authors contributed equally

[11]Lead contact

SUMMARY

*Correspondence: josejavier.bravo-cordero@mssm.edu.

AUTHOR CONTRIBUTIONS

C.M. designed and performed experiments, analyzed data, and wrote and revised the manuscript. K.A.L., M.J.G.-G., and R.C.A. performed zebrafish embryo experiments. C.-C.C. and A.G. performed atomic force microscopy and data analysis. J.S.Di.M., M.F., and I.E. helped to perform and analyze experiments. E.A.-P. and K.C. assisted with FLIM-FRET experiments. A.N. provided expertise on proteomics. U.O. performed data analysis. B.L.M. and D.Q.M. revised the manuscript for intellectual content. S.U., T.-M.F., and E.B. performed lattice light-sheet/adoptive optics microscopy and data analysis. J.J.B.-C. coordinated the study, contributed to designing and interpretation of the experiments, and wrote and revised the manuscript.

DECLARATION OF INTERESTS

A.N. receives research support for work unrelated to this study from Boehringer-Ingelheim. D.Q.M. is a paid consultant for Arcadia Science.

SUPPLEMENTAL INFORMATION

Supplemental information can be found online at https://doi.org/10.1016/j.celrep.2022.111358.

Many breast cancer (BC) patients suffer from complications of metastatic disease. To form metastases, cancer cells must become migratory and coordinate both invasive and proliferative programs at distant organs. Here, we identify srGAP1 as a regulator of a proliferative-to-invasive switch in BC cells. High-resolution light-sheet microscopy demonstrates that BC cells can form actin-rich protrusions during extravasation. srGA-P1^{low} cells display a motile and invasive phenotype that facilitates their extravasation from blood vessels, as shown in zebrafish and mouse models, while attenuating tumor growth. Interestingly, a population of srGAP1^{low} cells remain as solitary disseminated tumor cells in the lungs of mice bearing BC tumors. Overall, srGAP1^{low} cells have increased Smad2 activation and TGF-β2 secretion, resulting in increased invasion and p27 levels to sustain quiescence. These findings identify srGAP1 as a mediator of a proliferative to invasive phenotypic switch in BC cells *in vivo* through a TGF-β2-mediated signaling axis.

In brief

Disseminated tumor cells can remain quiescent or actively proliferate in distant organs, contributing to aggressive disease. Mondal et al. identify srGAP1 as a regulator of a proliferative-to-invasive decision by breast cancer (BC) cells through a TGF-β2-mediated signaling axis.

Graphical Abstract:

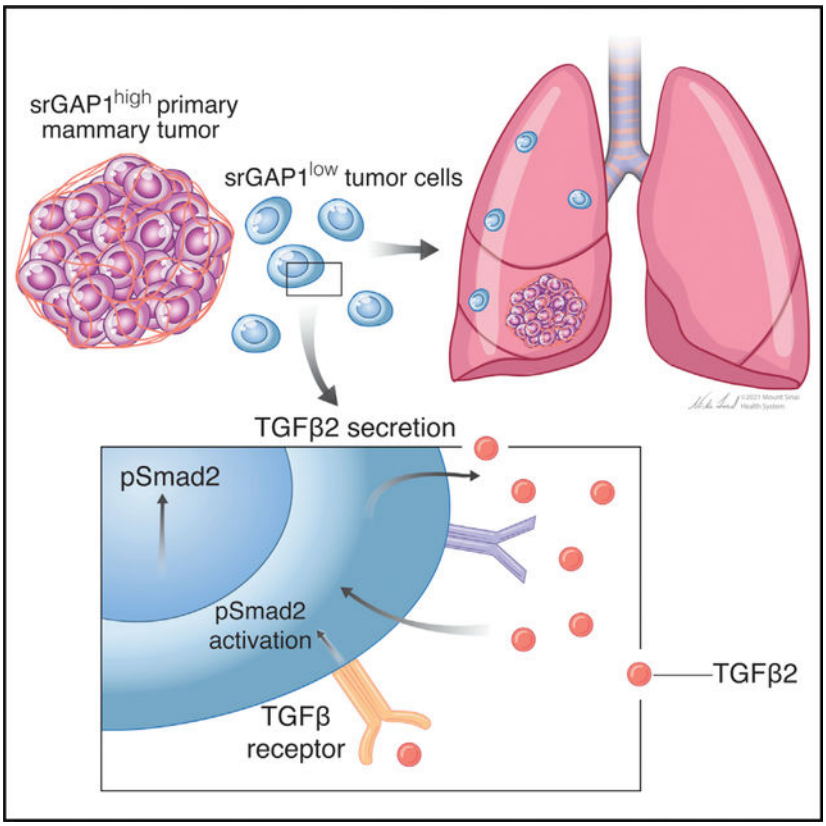

INTRODUCTION

Metastasis is a complex process during which cancer cells have to overcome several physical barriers (the extracellular matrix, vasculature) to arrive and proliferate at a distant site (Jiang et al., 2015; Lambert et al., 2017). From early tumor cell dissemination from the primary site to metastatic outgrowth, there is a potential time interval or latency period that can last years or decades (Aguirre-Ghiso and Sosa, 2018; Sosa et al., 2014).

Previous work has described mechanisms that regulate tumor cell migration and invasion in tumors (Condeelis and Segall, 2003; Friedl and Alexander, 2011; Friedl and Wolf, 2003; Mondal et al., 2020). A subset of cancer cells form invasive protrusions, termed invadopodia, that degrade the extracellular matrix (ECM) and facilitate invasion and intravasation into the blood vessels (Beaty and Condeelis, 2014; Eddy et al., 2017). Live-cell imaging studies have revealed that several actin cytoskeletal proteins localize at invadopodia structures and regulate their formation and matrix degradation function (Bravo-Cordero et al., 2011; Oser et al., 2009; Sharma et al., 2013; Stylli et al., 2009). Master regulators of invadopodia formation include RhoGTPases, as well as upstream GEFs and GAPs (Beaty and Condeelis, 2014; Spuul et al., 2014); however, the role of RhoGAPs during tumor cell dissemination is not well understood (Haga and Ridley, 2016). One subfamily of RhoGAPs, the srGAP (slit-robo GTPase-activating protein) family that consists of srGAP1, srGAP2, and srGAP3, and a related member ARHGAP4, is a key regulator of neuronal function. Despite the function of these proteins in controlling neuronal migration (Jordan et al., 2009; Wong et al., 2001), their role in invadopodia formation, tumor cell dissemination, and metastatic progression in breast cancer (BC) is vastly unknown.

Characterization of tumors deficient in invadopodia formation demonstrated that invadopodia are required for tumor cell intravasation in mouse models (Gil-Henn et al., 2013; Gligorijevic et al., 2012); however, tumor cell extravasation is not well characterized. Studies using a chicken chorioallantoic membrane model showed that invadopodia are necessary for cancer cell extravasation (Leong et al., 2014; Williams et al., 2019). In zebrafish, recent work using light-sheet microscopy revealed that cancer cells may extravasate by forming active protrusions that facilitate invasion through the endothelium (Liu et al., 2018) and has also been utilized to demonstrate how blood flow affects circulating tumor cell arrest and extravasation (Follain et al., 2018).

After tumor cells extravasate out of the vasculature, several molecular changes may occur for disseminated tumor cells (DTCs) to colonize and proliferate in distant organs (Obenauf and Massagué, 2015; Strilic and Offermanns, 2017). In certain cancers, a phenotypic switch between an invasive and proliferative state has been characterized; melanoma cells are capable of undergoing a proliferative-to-invasive phenotypic switch regulated by the transcription factor MITF and the tyrosine kinase receptor Axl (Arozarena and Wellbrock, 2019). When implanted *in vivo*, melanoma cell lines display heterogeneity of MITF levels, suggesting that these plastic states may be regulated by microenvironmental factors (Hoek et al., 2008). Thus, within a tumor, some cells may be more capable of switching between proliferative and migratory states to colonize organs efficiently. In the context of BC, the mechanisms regulating a proliferative-to-invasive switch have not been well explored.

Interestingly, intravital imaging studies in BC mouse models identified a subpopulation of cancer cells that display an invasive phenotype capable of intravasating into the blood stream (Condeelis and Segall, 2003; Harney et al., 2015; Patsialou et al., 2013; Roh-Johnson et al., 2014). Gene expression analysis of the invasive cell population revealed that, as cell motility genes are upregulated, several other cell-cycle genes are downregulated (Patsialou et al., 2012), suggesting that a phenotypic switch favoring invasiveness is governing the behavior of this BC cell population.

Once cancer cells seed at a distant site, they may enter into a period of dormancy that prolongs their latency before actively proliferating (Aguirre-Ghiso, 2007). Dormant cells are characterized by a reversible cell-cycle arrest in which they remain in a G0-G1 state until they restore proliferation (Aguirre-Ghiso, 2007). Several tumor microenvironment factors, such as TGF-β2, Bmp4, and others (Prunier et al., 2019), contribute to establishing dormancy at distant sites.

In this study, we investigate mechanisms that mediate a proliferative-to-invasive switch in BC cells. We identified srGAP1 as a negative regulator of tumor invasion and extravasation. srGAP1^{low} cells display a highly motile phenotype and become arrested in G0/G1 at distant organs, potentially prolonging their latency through the activation of a TGF-β2/Smad2 pathway.

RESULTS

srGAP1^{low} cells have increased extravasation from blood vessels

Using a matrix degradation assay as a readout for the invasive capability of BC cells, our data demonstrate that the silencing of neuronal GAPs, including the srGAP members, results in increased degradation of gelatin matrix in MDA-MB-231 BC cells (Figure S1A). Recent work has shown that several neuronal genes are mutated in different cancers (Logotheti et al., 2020), and some may regulate cancer progression (Ding et al., 2020; Mehlen et al., 2011); however, little is known regarding regulators of Rho GTPases in the context of tumor cell dissemination and metastasis. While recent literature points to the role of srGAP2 and srGAP3 in tumor and metastasis suppression (Lahoz and Hall, 2012; Marko et al., 2016), the role of srGAP1 in cancer is mostly unknown and not characterized in BC. In addition, srGAP3 has been shown to have low levels of protein expression in triple-negative BC (TNBC) cells (Lahoz and Hall, 2012). Thus, we decided to focus our studies on the role of srGAP1 in BC invasion and metastasis. Interestingly, we found that srGAP1 is highly enriched in TNBC cells, but has low expression in epithelial-like BC cells (Figure S1B), suggesting that srGAP1 may have BC subtype-specific functions.

BC cells can promote tumor cell invasion through the formation of invadopodia, which are F-actin-rich protrusive structures that focalize matrix metalloproteinases to degrade the extracellular matrix (Eddy et al., 2017). Seeding at distant organs requires cancer cells to extravasate from blood vessels, and evidence from past studies suggests that the formation of invadopodialike structures may facilitate extravasation (Leong et al., 2014; Williams et al., 2019).

To better understand the dynamics of invadopodia-like protrusions during extravasation, we utilized zebrafish embryos, which are optically transparent and amenable to xenografts of human tumor cells. Transgenic Tg(kdrl:RFP) embryos were injected with LifeAct-labeled MDA-MB-231 cells. Lattice light-sheet microscopy with adaptive optics was applied *in vivo* to study BC cell extravasation and actin dynamics. Our imaging approach revealed that BC cells in close proximity to blood vessels (white arrows) can form dynamic actin-rich finger-like protrusions that resemble invadopodia toward blood vessels (Figures 1A and 1B; Videos S1, S2, S3, and S4), while some other BC cells circulating in the blood remain non-protrusive and round in structure (yellow arrows). Once in close contact with the endothelial cells, cancer cells may form actin-rich invadopodia-like protrusions (Figure 1C; Videos S5 and S6) and extravasate out of the blood vessels (Figure 1D; Videos S7 and S8). Our data also demonstrate heterogeneity in tumor cells in the vasculature, including non-protrusive cells that are arrested in the vasculature (Figure S1C) and moving cells within the vasculature that are protrusive (Figure S1D).

Because srGAP1 loss promoted tumor cell invasion, we aimed to determine whether srGAP1 had a direct effect on tumor cell extravasation from blood vessels. Transgenic Tg(kdrl:RFP) embryos injected with GFP-labeled control or srGAP1-depleted tumor cells, herein, srGAP1^{low} tumor cells (Figures 1E, 1I, S1E, and S1F), demonstrate that srGAP1^{low} tumor cells have a greater propensity of exiting the vasculature than control cells (Figures 1E and 1F). When analyzing the percent extravasation we find that a higher percentage of srGAP1^{low} tumor cells are capable of extravasating out of the vasculature relative to control cells (Figure 1F), suggesting that srGAP1-depleted tumor cells can cross the endothelial barrier more efficiently. Time-lapse confocal microscopy visualizes srGAP1^{low} tumor cells within and outside the vasculature that are more elongated (Figure S1G) with long protrusions (Figures S1H and 1H) and protrusive activity (Figure 1G; Videos S9 and S10).

srGAP1 regulates matrix degradation and invadopodia dynamics

At the subcellular level, single-molecule imaging of cortactin, F-actin, and srGAP1 staining reveals that srGAP1 localizes in small clusters within invadopodia in MDA-MB-231 cells (Figure 2A). Time-lapse confocal imaging of MDA-MB-231 cells expressing LifeAct-Ruby and plated on gelatin matrices demonstrates that srGAP1^{low} cells with transient reduction of srGAP1 levels using siRNAs (Figure S2A) continuously degrade the extracellular matrix over time to a greater extent than control cells (Figures 2B, 2C, and S2B; Video S11). Interestingly, a similar effect was observed when cells were plated on a mixed fibrillar collagen I matrix (Figures 2D and 2E), suggesting that srGAP1^{low} cells are overall more effective at degrading the ECM relative to Ctrl cells. Similar results were obtained in BT549 TNBC cells (Figures S2C–S2E).

Because srGAP1 localizes to invadopodia and affects matrix degradation, we hypothesized that srGAP1 may affect the formation of invadopodia (Murphy and Courtneidge, 2011; Sharma et al., 2013). Invadopodia formation is spatiotemporally regulated; invadopodia precursors are assembled through the recruitment of several actin regulatory proteins, stabilize upon Tks5 arrival, and transition into maturation allowing for rapid F-actin

polymerization cycles and the recruitment of metalloproteinases (Beaty and Condeelis, 2014; Eddy et al., 2017). Loss of srGAP1 increases the number of cells capable of forming invadopodia as stained with cortactin and Tks5 (Figure 2F).

Mature invadopodia, which are capable of degrading the ECM, were measured through immunofluorescence of MDA-MB-231 cells plated on gelatin. Tks5- and cortactin-positive invadopodia on top of an area of matrix degradation (Figure 2G) were considered mature. srGAP1^{low} cells form more mature invadopodia than control cells (Figure 2H). When measuring the lifetime of mature invadopodia, srGAP1^{low} cells have a much shorter lifetime and a greater frequency of turnover than control cells (Figures 2I and 2J). Taken together, the combination of srGAP1^{low} cells forming more mature invadopodia with a high turnover rate may account for the overall increase in matrix degradation.

srGAP1^{low} cells show increased deformability, enhancing migration and invasion *in vivo*

We next asked whether the increase in matrix degradation by srGAP1^{low} BC cells accounts for greater cellular invasion. Using a transwell collagen I plug assay (Di Martino et al., 2017), we find that srGAP1^{low} cells can invade farther distances into the collagen I plug (Figures 3A–3C). The effects of srGAP1^{low} cells *in vitro* demonstrate that the loss of srGAP1 enhances matrix degradation and allows tumor cells to invade deep into collagen I plugs.

In vivo, tumor invasion requires matrix degradation along with cellular movement. To visualize whether srGAP1^{low} cells show increased invasion in an *in vivo* context, we injected GFP-labeled Ctrl and srGAP1^{low} cells (Figure S1E) orthotopically into the 4th mammary fat pad of immunodeficient mice (Figure 3D). Interestingly, when we performed intravital imaging on the primary tumors from control and srGAP1^{low} cells (Figures 3D and 3E; Videos S12 and S13), GFP-labeled srGAP1^{low} tumor cells migrated from the primary tumor at a higher speed than control cells (Figure 3F). srGAP1^{low} tumor cells migrate farther distances than control cells, but maintain the same persistence ratio (Figures 3G and 3H), suggesting that GFP-srGAP1^{low} tumor cells are not migrating randomly, but in a directed and rapid manner. Similar results were obtained in 2D assays *in vitro* (Figure S3A–S3E). These results demonstrate that srGAP1^{low} cells have increased matrix degradation and migration to facilitate tumor invasion *in vivo*.

Analysis of the biomechanical properties of cancer cells have shown that invasive cancer cells are softer and more deformable than non-invasive cancer cells (Lekka et al., 2012). Recent studies have also shown that a decrease in stiffness contributes to higher migration speeds (Han et al., 2020). To characterize cell mechanics in control and srGAP1^{low} cells, we used atomic force microscopy and measured the elastic properties of individual BC cells. We measured the Young's elastic modulus as a measure of cellular deformability by taking a series of individual measurements per cell (Figure 3I). Our data show that srGAP1^{low} cells were softer than the controls (Figure 3J), suggesting that the increase in cellular softness of srGAP1^{low} cells contribute to the increased migration observed *in vivo*.

To gain more insight into the signaling pathways that are regulating srGAP1^{low} motility and invasive phenotypes, we performed an RNA sequencing (RNA-seq) analysis (Figure

S4A; Table S1) on control and knockdown primary tumors from the MDA-MB-231 xenografts. GO analysis shows that srGAP1^{low} tumors have a significant number of genes that are differentially expressed involving RhoGTPase signaling (Figure S4B). Interestingly, FLIM-FRET experiments using RhoA, Cdc42, and Rac1 biosensors revealed that loss of srGAP1 results in decreased RhoA activation (Figure S4C), and does not affect Cdc42 or Rac1 activation at the leading edge when compared with control cells (Figures S4D and S4E), suggesting that other GAPs may be controlling the cycling of these GTPases, besides srGAP1. Several studies analyzing the biomechanical properties of cells upon RhoA inhibition show a decrease in stiffness (Sharma et al., 2014; Wagh et al., 2008), similar to our atomic force microscopy measurements. Moreover, our transcriptomics analysis revealed a significant upregulation of other GAPs in srGAP1^{low} cells (Figure S4F), which may contribute to their reduced RhoA activity and increased softness.

srGAP1^{low} cells show increased DTC seeding at distant organs, but reduced metastatic outgrowth

Surprisingly, while performing intravital imaging of srGAP1^{low} tumors, we found that mice bearing srGAP1^{low} BC cells had a reduction in tumor growth compared with control tumors, as demonstrated by measuring tumor volume (Figures S5A and S5B) and mass (Figures S5C and S5D). In addition, tumor latency, measured as the elapsed time between the injection of BC cells and the moment a tumor is palpable was longer in srGAP1^{low} tumors (Figures S5E). No increase in apoptosis was observed (Figure S5F), and there is an increase in the percent of srGAP1^{low} cells in G0/G1 and a decrease in G2 (Figures S5G and S5H). These results, along with the significant increase in invasive capacities of srGAP1^{low} cells described previously (Figures 1, 2, and 3) led us to hypothesize that srGAP1 could be a regulator of a proliferative-to-invasive switch and may control DTC proliferation at metastatic organs.

When examining the lungs (Figures 4A–4C and S4G) of mice bearing control or srGAP1^{low} tumors, we found that more srGAP1^{low} tumor cells were able to seed distant organs than control cells (this same increase in seeding was observed when lungs from Ctrl tumors were analyzed at the time the tumor size was similar to the srGAP1^{low} tumors, suggesting that dissemination is an early event in srGAP1^{low} tumors due to their increase in motility Figures S4G and 3F). However, when examining overt metastases, which indicates tumor cell outgrowth, srGAP1^{low} mice show a significant growth defect in metastatic lesions, with reduced overall metastatic burden in the lung (Figure 4D). In addition, of the seeding events in the lung, srGAP1^{low} mice have a greater proportion of single cells in both the lung (Figures 4E and 4F) and the liver (Figure S5I).

Solitary DTCs are srGAP1^{low} and remain in G0/G1 arrest

To directly determine whether srGAP1 levels may identify a population of DTCs in the lungs of mice bearing BC tumors that may remain in a non-proliferative state, we immunostained lung sections from control MDA-MB-231 human xenografts with an srGAP1-specific antibody (Figure S5J). Our results show that single, solitary cells have lower srGAP1 expression than micrometastasis (Figures 5A and 5B), suggesting that low levels of srGAP1 maintain DTCs in a non-proliferative state.

To assess how srGAP1 restricts both primary tumor growth and metastatic outgrowth, we utilized a DHB:Venus sensor that measures Cdk2 activity and marks the progression of the cell cycle (Spencer et al., 2013). When cells are in a G0/G1 state, the DHB:Venus sensor remains in the nucleus; as the cell progresses through the cell cycle, Cdk2 activity increases and the sensor is exported out of the nucleus into the cytoplasm (Figure 5C, bottom). Live-cell imaging experiments with a DHB:Venus sensor shows srGAP1^{low} cells have prolonged accumulation of the sensor in the nucleus (with an overall lower cytoplasmic/nuclear ratio), suggesting that the cells remain in a G0/G1 arrest (Figures 5D and 5E; Video S14). In addition, analysis of control and srGAP1^{low} cells in the lungs reveals an increase in the number of srGAP1^{low} cancer cells in the G0/G1 phase of the cell cycle (Figures 5F and 5G). Overall, these data reveal that srGAP1^{low} DTC cells remain as solitary and G0/G1-arrested cells in the lungs.

Increased TGF-β2 levels activate Smad2 in srGAP1^{low} cells and increase matrix degradation

KEGG pathway enrichment analysis and Reactome pathway analysis demonstrate that TGF-β signaling is altered in srGAP1^{low} tumors compared with control tumors (Figure 6A). Immunofluorescence staining and western blot analysis show an increase of Smad2 total levels as well as increased nuclear Smad2 in srGAP1^{low} cells, and no change in Smad3 levels (Figures 6B, 6C, 6D, and S6A). Previous studies have shown that activation of Smad2, upon TGF-β stimulation, triggers Smad2 phosphorylation and nuclear translocation (Derynck and Budi, 2019). We performed immunofluorescence analysis of pSmad2 and found increased levels of nuclear pSmad2 upon srGAP1 knockdown (Figure 6E). To determine whether an increase in TGF-β levels may be contributing to Smad2 activation in a cell-autonomous manner, we performed a secretome analysis of the conditioned medium (CM) from control and srGAP1^{low} cells (Figures 6F and S6I;, Table S2). Analysis of the secretome of srGAP1^{low} BC cells reveals that secreted proteins are enriched in categories related to cell cycle, metabolism, and G-protein signaling compared with the secretome of control cells (Figure 6G).

Interestingly, srGAP1^{low} cells secrete an increased amount of TGF-β2 when compared with Ctrl cells (Figure 6H). We validated these results by performing a TGF-β1–3 Luminex assay, and found that, while srGAP1^{low} cells secrete increased TGF-β2, they secrete less TGF-β1 and have no change in TGF-β3 secretion when compared with Ctrl cells (Figures S6B–S6G). Previous studies have shown that TGF-β2 signaling has been shown to induce dormancy of cancer cells (Bragado et al., 2013), suggesting that activation of this pathway in srGAP1-depleted cells contributes to their prolonged latency observed *in vivo* (Figures 4 and 5).

We wanted to determine if the secretome of srGAP1 cells contributes to the invasive properties observed in srGAP1^{low} BC cells. Culture of MDA-MB-231 cells with CM from srGAP1^{low} cells show an increase in matrix degradation when compared with treatment with conditioned medium from control cells (Figure S6H). Previous work has shown that TGF-β stimulation can activate the invasion of MCF10A cells (Pignatelli et al., 2012). Given the observed increase in TGF-β2 in the CM of srGAP1^{low} cells, we hypothesize that TGF-β2

may contribute to the increase in invasion of cancer cells. Upon TGF-β2 treatment, BC cells show a significant increase in matrix degradation (Figures 6I and 6J). Moreover, *in vivo*, primary tumors with low srGAP1 levels have an increase in nuclear p27 staining (Figures 6K and 6L), which has been shown to be upregulated downstream of TGF-β2 signaling to maintain tumor cell quiescence (Bragado et al., 2013). To determine whether the increase in secreted TGF-β2 from srGAP1^{low} cells was due to growth arrest, we serum starved MDA-MB-231 cells and examined TGF-β2 expression by immunoblotting and found a reduction in starved cells (Figures S6J and S6K), suggesting that changes in TGF-β2 levels are due to a srGAP1^{low}- specific program. Interestingly, analysis of RNAseq data show that srGAP1^{low} cells have high levels of the TGF-βRIII ($\log_2$fold change = 1.06, $p_{adj} = 6.19 \times 10^{-6}$), previously linked to dormancy in head and neck models (Bragado et al., 2013).

We then investigated the role of TGF-β2-mediated signaling on srGAP1^{low}-dependent phenotypes. Using an siRNA to deplete TGF-β2 from srGAP1^{low} cells, there is a significant reduction in matrix degradation (Figures 7A and 7B). In addition, treating srGAP1^{low} cells with a small-molecule inhibitor of TGF-βRI results in less matrix degradation, suggesting that the TGF-β2-TGF-βRI signaling axis may regulate invadopodia function. As srGAP1^{low} cells are more efficient at extravasation, we depleted TGF-β2 from srGAP1^{low} cells and injected them into the tail vein of immunodeficient mice and found a reduction of extravasation (Figures 7D and 7E), demonstrating the necessity of TGF-β2-mediated signaling for invasive events. We also examined the contribution of TGF-β2 to srGAP1^{low} cell-cycle arrest with the DHB:Venus sensor for Cdk2 activity, and found that, upon depletion of TGF-β2, srGAP1^{low} cells escape the G0/G1 state (Figures S7A and S7B), suggesting that TGF-β2 may contribute to the slow cycling nature of srGAP1^{low} cells.

All together, these results demonstrate that srGAP1^{low} cells have increased TGF-β2/Smad2 signaling, leading to an increase in matrix degradation along with an increase in p27, suggesting prolonged quiescence/dormancy.

DISCUSSION

The first report linking srGAP1 to cancer was a study in papillary thyroid carcinoma (PTC) in which the authors described srGAP1 as a candidate susceptibility gene for PTC (He et al., 2013). Since that, several studies linked the downregulation of srGAP1 with increased invasion. A study in glioblastoma showed that downregulation of srGAP1 expression through overexpression of miR-145 increased invasion (KOO etal., 2015). In another study in colorectal cancer, downregulation of srGAP1 was associated with increased lymphatic invasion (Feng et al., 2016). On the other hand, in gastric cancers, srGAP1 is upregulated through miR-340 and miR-124 downregulation, promoting metastasis (Huang et al., 2018).

In the context of BC, the role of srGAP1 was completely unknown. Interestingly, in human ER$^-$/PR$^-$ BC, analysis of expression levels for srGAP1 showed that relapse-free survival was significantly higher in the patient group of low srGAP1 expression, as shown by a Kaplan-Meier plot, and overall survival is reduced in all BC patients as well as in ER$^-$/PR$^-$ patients (Figures S7C–S7E). Our data describing the long latency of srGAP1^{low} tumors may

explain these clinical results and suggest that srGAP1 expression is prognostic of survival in ER^-/PR^- BC patients.

Several studies described an invadopodia-dependent function for extravasation (Gil-Henn et al., 2013; Gligorijevic et al., 2012; Leong et al., 2014; Williams et al., 2019). Our study reveals srGAP1 as a new regulator of invadopodia function and tumor cell extravasation. Moreover, in our zebrafish experiments we observed that extravasated $srGAP1^{low}$ cells display multiple cellular protrusions, suggesting that downregulation of srGAP1 may contribute to the establishment of connections with other niche components to efficiently seed at metastatic sites.

We demonstrate that srGAP1 regulates a proliferative-to-invasive switch, which is not a well-characterized phenomenon in BC. In certain tumors, invasion has been correlated with a decrease in cell proliferation (Hoek et al., 2008; Kohrman and Matus, 2017; O'Connell and Weeraratna, 2013; Widmer et al., 2013). For example, in BC cell lines, Arg/Abl2 was shown to attenuate cell proliferation in primary tumors and promote invasion through invadopodia regulation (Gil-Henn et al., 2013). Recent studies in BC cells have also shown that matrix degradation by invadopodia is enhanced in the G1 phase of the cell cycle (Bayarmagnai et al., 2019).

During development, *C. elegans* anchor cell (AC) invasion (a specialized uterine cell) has been used as a model to understand the process of invasion through basement membranes (BMs) (Hagedorn and Sherwood, 2011; Sherwood and Sternberg, 2003). In many aspects, ACs resemble a cancer cell crossing a BM. ACs form invadopodia, with similar actin regulatory molecules as the ones found in tumor cells, that breach the BM (Lohmer et al., 2014) while remaining arrested in the G1 phase of the cell cycle (Matus et al., 2015) similar to our data presented here. These studies highlight the potential of using model organisms to identify new molecules that could play a role in tumor dissemination, and suggest that tumor cells may co-opt developmental processes during invasion and have a more complex role in the proliferative-to-invasive decision (Kohrman and Matus, 2017).

In glioma, a study found mitochondria localized within invadopodia structures (Arismendi-Morillo et al., 2012) and work on *C. elegans* ACs showed mitochondria localization at invasive protrusions to facilitate BM invasion (Kelley et al., 2019). We can hypothesize that invading cancer cells will polarize their energy resources at invadopodia to meet the energy demands required for invasion (i.e., actin polymerization) while decreasing the energy required to engage in other cellular processes, such as cell division.

Our data also suggest that highly motile cancer cells with low levels of srGAP1 may be more prone to enter into a state of dormancy. Tumor cell dormancy maintains DTCs in a non-proliferative state for years or decades before they restore growth (Aguirre-Ghiso and Sosa, 2018; Sosa et al., 2014). The dormant cancer state is characterized by a reversible growth arrest where cells remain in the G0 phase of the cell cycle through interactions with the tumor microenvironment (Prunier et al., 2019). TGF-β2 has been identified as one of the mediators of the dormancy program through TGF-βRIII (Bragado et al., 2013; Nobre et al., 2021). Interestingly, RNA-seq analysis of dormant cells in a head and neck cancer model

also shows reduced levels of srGAP1 expression compared with proliferative cells (data not shown). Moreover, migratory, invasive tumor cells have been demonstrated to have nuclear expression of Smad2/3 by immunofluorescence when compared with “average primary tumor cells” (Patsialou et al., 2012), adding to the significance of TGF-β-mediated signaling in regulating invasion. Our study suggests that srGAP1 downregulation may contribute to tumor dormancy by establishing a TGF-β2-rich niche in a cell-autonomous manner. Interestingly, analysis of patient datasets demonstrates an anti-correlation between srGAP1 gene expression and TGF-β2 gene expression in BC patient samples (Figure S7E).

In summary, we have identified a novel signaling axis involving srGAP1^{low}/TGF-β2/Smad2 acting on invadopodia formation and invasion while regulating tumor cell proliferative capacities. Our data emphasize the importance of considering phenotypic changes that could occur when treating cancer cells with therapeutic strategies that target proliferating cells, such as chemotherapy. While these treatment regimens target dividing cells, they may also be selecting for more invasive tumors. Our studies suggest that more selective therapeutic strategies combining treatments against both dividing cells and non-dividing invasive cells may be necessary to prevent metastatic disease.

Limitations of the study

In this study, we identified a population of disseminated BC cells that have low srGAP1 expression. We investigated the consequences of srGAP1 loss in mammary tumors; however, we recognize that the mechanisms driving srGAP1 downregulation within tumors were not explored. In addition, while we described an upregulation of TGF-β2 secretion in srGAP1^{low} cells and activation of the Smad2/3 pathway, the mechanistic details describing how srGAP1 controls TGF-β2 secretion were not investigated. We anticipate that studies describing how srGAP1 regulates TGF-β2 secretion will be highly informative for the understanding of the role of srGAP1 during tumor dissemination.

STAR★METHODS

RESOURCE AVAILABILITY

Lead contact—Further information and requests for resources and reagents should be directed to and will be fulfilled by Jose Javier Bravo-Cordero (josejavier.bravo-cordero@mssm.edu).

Materials availability—This study did not generate any new, unique reagents.

Data and code availability

- RNAseq data have been deposited at GEO and are publicly available as of the date of publication. Accession numbers are listed in the key resources table. Proteomics data have been deposited at PRIDE and are publicly available as of the date of publication. Accession numbers are listed in the key resources table.
- This paper does not report original code.

- Any additional information required to reanalyze the data reported in this work paper is available from the lead contact upon request.

EXPERIMENTAL MODEL AND SUBJECT DETAILS

Cell lines—MDA-MB-231 and MCF7 were purchased from ATCC and cultured in 1X DMEM with 4.5 g/L D-Glucose and Glutamax (Gibco), and 10% fetal bovine serum (Gemini Bio, Cat #: 900–108). BT549 and HS578 T were kindly provided by the Condeelis lab (Albert Einstein College of Medicine, USA) who purchased the cells from ATCC. BT549 and HS578 T were cultured as above with insulin supplementation (0.023 units/mL insulin for BT549, 0.288 units/mL insulin for HS578 T). T47D were cultured in RPMI and 10% fetal bovine serum in 0.2 Units/mL insulin. HEK293 cells were used to generate lentivirus and were cultured in DMEM with 4.5 g/L D-Glucose and Glutamax (Gibco) and 10% fetal bovine serum (Gemini Bio, Cat #: 900–108). All cells were maintained at 37°C and 5% CO_2.

Mouse xenograft models—All experiments were conducted in accordance with the National Institutes of Health guidelines and were approved by the Icahn School of Medicine at Mount Sinai IACUC committee. 6-to-8 week old female immunodeficient NCG mice (NOD-*Prkdc*^{em26Cd52}*Il2rg*^{em26Cd22}/NjuCrl, Charles River Labs, Wilmington MA) and 8-to-10 week old female immunodeficient nu/nu mice (Crl:NU-*Foxn1*^{nu}, Charles River Labs, Wilmington MA) were used for mouse tumor xenograft and tail vein studies, respectively.

Zebrafish xenograft model—Adult zebrafish (*Danio rerio*) were maintained and crossed under standard conditions. Embryos were obtained from the transgenic line tg(*kdrl*:RFP) and were kept at 28.5°C during 48 h postfertilization (hpf). To avoid melanocyte formation, 200 μM N-Phenylthiourea (PTU) (Alfa Aesar) was added into the embryo media at 6 hpf and changed every 24hr. All zebrafish experiments and procedures were performed as approved by IACUC at Stony Brook University and Janelia Research Campus.

METHOD DETAILS

Plasmids/reagents—pHIV-H2B-mRFP was purchased from Addgene (#18982) for stable H2B-RFP expression, FG12-GFP was kindly provided by the Soengas lab (CNIO, Spain) (Olmeda et al., 2017) for stable GFP expression, CSII-EF-DHB-Venus (sensor for Cdk2 activity) was kindly provided by the Spencer lab (University of Colorado, USA) for cell cycle analysis, and a pLifeact-mRuby lentiviral vector was kindly provided by the Moreau and Saltel laboratories (DR2 INSERM, France) as in (Juin et al., 2014) for imaging actin dynamics. CFP-YFP RhoA biosensor (Pertz et al., 2006), a CFP-YFP Cdc42 biosensor (Hanna et al., 2014), and a CFP-YFP Rac1 biosensor (Miskolci et al., 2016) were kindly provided by the Hodgson lab (AECOM, USA). Recombinant Human TGF-beta 2/TGFβ2 Protein was purchased from AbClonal (RP00452) and diluted according to manufacturer's instructions. LY364947 (Selleck Chemical, S2805), an ATP-competitive inhibitor of TGFβR-I was diluted according to manufacturer's instructions.

Antibodies—For immunoblotting, primary antibodies were diluted in 5% BSA in 1X TBST or Odyssey Buffer (LiCOR) and added overnight at 4°C: Rabbit anti-srGAP1

(Bethyl Labs, A301–286A, 1:1000), Rabbit anti-srGAP2 (Abcam, ab124958, 1:1000), Rabbit anti-Smad2/3 (CST, 8685 T 1:1000), Mouse anti-alpha-tubulin (Sigma, T6074, 1:5000–1:10,000), Rabbit anti-Beta-actin (Abcam, ab8227, 1:5000–1:10,000), Rabbit anti-TGFβ2 (Abclonal, A3640, 1:1000). For immunofluorescence on cells, primary antibodies were diluted in 1% BSA in 1X PBS and added overnight at 4°C: Rabbit anti-srGAP1 (Proteintech, 13252–1-AP, 1:500), Rabbit anti-Cortactin (Abcam, ab81208, 1:50), Mouse anti-Tks5 (Millipore clone 13H6.3, MABT336, 1:50), Mouse anti-Cortactin (Millipore clone 4F11, 05–180-I, 1:300), Rabbit anti-Smad2/3 (CST, 8685 T, 1:100), Rabbit anti-pSmad2 (CST, 3108 S, 1:100), Mouse anti-Smad2 (1:100, LSBio, LS-C169392), and AlexaFluor labelled-secondary antibodies were diluted in 1% BSA in 1X PBS from 1:250–1:400. For immunofluorescence on tissues, primary antibodies were diluted in 1% donkey serum in 0.5% Tween 20 in 1X PBS and added overnight at 4°C: Chicken anti-GFP (Aves Labs, GFP-1010, 1:300), Rabbit anti-srGAP1 (Proteintech, 13252–1-AP, 1:100), Goat anti-p27 (LSBio, LS-B3943, 1:100), Rabbit anti-p27 (CST, 3686 S, 1:100).

Immunoblotting—Cells were lysed in modified RIPA buffer (0.1% SDS, 1% NP40, 150 mM NaCl, 1% sodium deoxycholate, 25 mM Tris-HCl pH 7.4) containing protease inhibitors (Complete Mini EDTA-free tablets; Roche) and phosphatase inhibitors (PhosSTOP, Roche). Protein concentrations were measured with a Lowry Assay (Bio-Rad), and 20–60 μg of protein was run on 8–10% SDS-PAGE gels. Protein was transferred on to a 0.45 μm nitrocellulose membrane (Bio-Rad) using a wet transfer or with Trans-Blot Turbo system, blocked for 1 h at room temperature in 5% BSA in 1X TBST or Odyssey Blocking buffer, and probed with antibodies diluted in 5% BSA in 1X TBST or Odyssey buffer. Mouse and rabbit near-infrared fluorescent secondary antibodies (LI-COR Biosciences) were added for 1 h at room temperature. The membrane was subsequently washed in 1X TBST, and imaged with an Odyssey CLx imaging system. Analysis was done with FIJI (Schindelin et al., 2012) by calculating densitometry relative to the loading control.

Lentiviral packaging and infection—Lentiviral transfer plasmids and plasmids encoding VSV-G, Gag-Pol, Rev, and Tat genes were transiently transfected with Lipofectamine™ 2000 (Thermo Fisher Scientific) into HEK293 T cells to package lentivirus. Lentivirus was packaged at 37°C and supernatant was collected after 48 h. Cell lines were infected with virus for 24 h and cultured to 80% confluence. Cells stably expressing fluorescent protein or biosensors were trypsinized, filtered with 40 μm cell strainers, and sorted in 1X PBS +2% FBS with a CSM4L sorter (BD Biosciences).

siRNA and shRNA—siRNAs were synthesized by IDT and transfected into cells with Lipofectamine RNAimax (Invitrogen) using the manufacturer's protocol. Cells were transfected for 96 h with 100 nm of siRNAs targeting human srGAP1 and a non-targeting control. siRNAs for human srGAP1 are as follows: si #1, 5′-GCAGAUAAGUGAGGAUUCU-3′, si #2, '5-CAUGAGGGCUUAGACAUUA-3′. The human TGFβ2 siRNA is a Silencer™ Select Pre-Designed siRNA, s14061. For the siRNA screen, a custom Qiagen siRNA FlexiPlate (0.25 nmol) was designed and used as described above. shRNAs for stable knockdown of human srGAP1 are as follows: KD #1, 5′-CCGCTCAC AGTATAATACTAA-3′, KD #2, 5′GCCCTGTTTATGAGAAATGTA-3′ in

a pLKO.1 vector. Control and knockdown cells with stable expression were selected for with 1.5 μg/mL puromycin for three days, and then expanded. Knockdown levels were checked with immunoblotting.

Zebrafish xenograft experiments

Injection of human cells: Zebrafish embryos were manually dechorionated and anesthetized with 0.003% tricaine (Pentair, TRS1) at 48 hpf. MDA-MB-231 cells were loaded in a glass capillary and injected with a CellTram® 4r Oil microinjector into the zebrafish blood stream via Duct of Cuvier (200–400 cells per fish). After the injection, the embryos were maintained in embryo media with 200 μM PTU at 33°C.

Image acquisition and processing: At 24 h post injection (hpi), embryos with tumor cells in the caudal hematopoietic tissue were selected for subsequent experiments. The engrafted embryos were anesthetized with tricaine 0.003% and mounted in a drop of 0.8% low melting agarose containing 0.003% tricaine in 35 mm glass bottom dish with uncoated #1.5 coverslip and 20 mm glass diameter (MatTek) for confocal and widefield microscopy or on round coverslip for light sheet microscopy. The embryos were manipulated with an eyelash tool for proper positioning. The embryos were then covered with 0.006% tricaine in embryo media.

To obtain the stitched whole tail, data images were acquired on either a widefield or confocal microscope. For widefield images a Nikon Eclipse Ti inverted epifluorescence microscope was used equipped with an Andor Zyla camera, a Lumencor SPECTRA X LED light engine with a DIC 20×/0.75 NA objective. Z-stacks were acquired every 2 μm, binning was set to 1 3× 1 with an exposure of 50 ms for G/Y and 200 ms R. For confocal imaging a custom-assembled spinning disk system was used consisting of a Zeiss Axio Imager A2 inverted frame with a Yokogawa CSU10 spinning disk, an ASI filter wheel, a Prime 95b sCMOS camera, a 6-line laser merge by Vortran and a 25×/0.8 NA multi-immersion objective (Carl Zeiss) with oil immersion. Z-stacks were acquired every 3 μm with 25 mW and 200 ms exposure for 561 nm and 488 nm. The acquired tiled z-stacks were max projected in Fiji/ImageJ (Schindelin et al., 2012) and then either stitched in Fiji/ImageJ using the pairwise stitching plugin (Preibisch et al., 2009) or by hand.

Live imaging of each cell in the caudal hematopoietic tissue was carried out using a custom assembled spinning disk confocal microscope consisting of a Zeiss Axio Imager A2 frame, a Borealis modified Yokogawa CSU10 spinning disc, an ASI 150-micron piezo stage controlled by a MS2000, an ASI filter wheel, a 6-line laser merge system from Vortran and a Hamamatsu ImageEM X2 EM-CCD camera. The imaging objective used was either a Plan Apochromat 40×/1.0 NA or 63×/1.0 NA water dipping objective (Carl Zeiss). Z-stacks were acquired every 1 μm with 488 nm and 561 nm with 2–5 mW and 200–300 ms exposure with a gain set at 80–100. For long timelapse data Z-stacks were acquired every 5 min and to capture extravasation a single Z was imaged every 500msec- 3sec. Images were then de-identified to blind the image analyst to the data and scored for intravasation vs. extravasation using the orthogonal and 3D viewing in Fiji/ImageJ (Schindelin et al., 2012). Plots were generated using GraphPad Prism.

Lattice light sheet microscopy with adaptive optics correction—Zebrafish samples were anesthetized (0.003% tricaine) and embedded in low melt agarose (0.8%) on a 25 mm coverslip. The excitation and detection objectives together with the coverslip were immersed in ~40 mL of fish water at 33°C. Prior to time series data acquisition, the image volume was corrected for optical aberrations using two-photon guide star based adaptive optics method. With aberration-corrected mirror patterns, simultaneous two-color (488 nm and 560 nm) time-lapse lattice light sheet imaging with an outer/inner numerical aperture of 0.4/0.3 was then performed. The emission light was separated by a long-pass filter (Di03-R561-t3, Semrock) and captured by two sCMOS cameras (ORCA-Flash 4.0 sCMOS, Hamamatsu Photonics). Volumetric imaging was done by axially scan the samples with a step size of 250 nm. Each imaged volume was deconvolved with experimentally obtained point spread functions measured from 100 nm tetraspec beads (Thermo Fisher) in C++ on HHMI Janelia Research Campus' computing cluster. Image analysis was performed using FIJI (Schindelin et al., 2012) and Imaris.

***In vivo* mouse experiments—**Xenograft models: 1 × 10^6 cells MDA-MB-231-GFP cells were suspended in 100 μL of sterile 1X PBS and injected into the fourth mammary fat pad of 6-to-8 week-old NCG mice (Charles River Labs, Wilmington MA). Mice were assessed for body condition score and weighed twice a week. Tumor growth for the knockdown cell lines was measured as soon as tumors were palpable with a caliper. Formula for tumor volume: $V = W^2 \times L/2$ (W: width, L: length). Mass of tumors was measured at 6 weeks. Tail-Vein Injections: 400,000 GFP-labelled MDA-MB-231 cells in 100 ul of 1X DPBS were injected into the tail-vein of immunodeficient mice with an insulin syringe. Images of the lungs were acquired 48–72 h post-injection with an Olympus FVMPE-RS Multiphoton microscope.

Immunofluorescence—Cells were fixed in 4% paraformaldehyde in 1X PBS, permeabilized with 0.2% Triton X- in 1X PBS for 5 min, and blocked with 10% BSA in PBS for 1 h. Primary antibodies were added overnight at 4°C in 1% BSA in PBS, and secondary antibodies and/or phalloidin for F-actin-labeling for 1 h at room temperature in 1% BSA in PBS. DAPI (1–10 μg/mL, Biotium) was added in the last wash to label nuclei. Coverslips were mounted with Fluoromount-G™ Mounting Medium (Thermo Fisher Scientific).

Matrix degradation assays—Glass coverslips were coated with 1 mg/mL Alexa Fluor 488 or 546-labelled gelatin matrix as in (Di Martino et al., 2017). Cells were plated on coverslips, fixed with 4% PFA in PBS at 4 h or 16 h, and stained with DAPI, cortactin and/or phalloidin. For mixed matrices with fibrillar collagen on Alexa Fluor 546-labelled gelatin, 0.5 mg/mL collagen I (BD Biosciences) was polymerized in DPBS +/+ for 4 h on top of gelatin. Cells were plated immediately on the mixed matrix, and fixed 16 h later. Images were acquired with a widefield Leica DM300 upright microscope with a DFC345X camera and an HCX PL APO 100× NA 1.4 objective. Matrix degradation area per field was quantified with FIJI (Schindelin et al., 2012). Measurements were acquired by thresholding matrix degradation and dividing by the number of cells per field (as demarcated with DAPI staining) (Di Martino et al., 2017).

Live-cell imaging—Cells were plated on either 1 mg/mL fluorescent gelatin matrix (Thermo Fisher) or fibrillar collagen I for 2–4 h and then imaged in L15 phenol-red free media (Gibco) with 10% FBS (Gemini Bio) using an inverted confocal Zeiss LSM 880 microscope. Imaging was conducted in a 37°C humidified and temperature-controlled chamber. Z-stacks were acquired every 30 min for 24 cycles with a 63X 1.4 NA objective, with a z-step size of 0.8–1 μm. Analysis of cell motility parameters was done with Imaris (Bitplane, Switzerland).

Collagen I plug assay—Collagen I plugs were prepared as in (Di Martino et al., 2017). Briefly, Alexa Fluor 546 NHS-ester was added to rat-tail collagen I (Corning), and mixed with PBS and 1 M NaOH for a final concentration of 2 mg/mL. The collagen I solution was added to cell culture inserts and allowed to polymerize for 1 h at 37°C. Plugs were enriched in 50% serum/1X DMEM for 4 h at 37°C, and 2.5 × 10^4 cells were plated on top of the plugs in serum-free media. Inserts were placed in complete media (1X DMEM with 10% FBS), and plugs were fixed with 4% PFA in PBS at 30 min and 3 days after seeding. Z-stacks of plugs were imaged with a Leica TCS SP5 DMI inverted microscope with a 40× NA 1.25 objective.

Multi-color dSTORM—Samples were fixed on #1.5H coverslips, stained, and immersed in ONI's bCubed STORM buffer and placed on a cavity slide. The images were acquired using a 100X 1.4 NA Olympus objective on the Nanoimager S (Oxford NanoImaging, ONI, Oxford, UK) with lasers 405 nm/150 mW, 488 nm/1000 mW, 561 nm/500 mW, 640 nm/1000 mW and dual emission channels split at 640 nm. The signals from Alexa 647, Alexa 555, and Alexa 488, or Alexa 647 and Alexa 488 only, were recorded sequentially for 10,000 frames each using 100% laser power onto the dual-color channel sCMOS camera (Hamamatsu Orca Flash 4.0 V3). For localization of the individual molecules, the Nanoimager software v.1.4 was used to localize the molecules by fitting detectable spots of high photon intensity to a Gaussian function. The final image reconstruction was displayed in precision mode.

Fluorescence lifetime imaging (FLIM) acquisition and FLIM-FRET analysis—FLIM experiments were carried out on cells transiently transfected with either a CFP-YFP RhoA biosensor (Pertz et al., 2006) or a CFP-YFP Cdc42 biosensor (Hanna et al., 2014) and fixed on coated coverslips. Time-correlated single photon counting FLIM was performed with a Leica TCS SP8 two-photon FALCON (Fast Lifetime CONtrast) system. A SpectraPhysics Insight X3 tuned to 850 nm pulsed laser source was used at 1.5%, and an NDD Hybrid detector was used for detection. Images were acquired with a 40X, NA 1.10 HC PL IRAPO objective, and were scanned at 600 Hz with a zoom of 3.75. The measured decay curve was fitted to a multiexponential curve using the FALCON software. The fluorescence lifetime was calculated per pixel for the donor molecule of the FRET pair. A custom FIJI macro (adapted from EdgeRatio, https://cail.cn/code/EdgeRatio.txt) was written to calculate the mean fluorescence lifetime of a particular ROI (10 μm × 10 μm) at the leading edge of the cell. Two 10 μm × 10 μm regions were selected at the edge of the cell; measurements are calculated from the edge of the cell up to 2 μm inwards from 1 z-slice. The Rac1 biosensor FLIM images were captured with LAS X software

(Leica Application Suite X 4.3.0.24308) on a Leica Stellaris 8 (Leica Microsystems GmbH, Wetzlar, Germany) confocal microscope equipped with 4 spectral PowerHyD and TauSense technology. Imaging was performed using 40×/1.3 HC PlanApo oil immersion lens (Leica Microsystems GmbH, Wetzlar, Germany) and an optical zoom of 4, the frame size was set to 512 × 512 pixels (X/Y) for the final lateral pixel size of 0.142 um/pixel, and images were acquired at 8bits. The acquisition was performed at frame scan mode, with a pixel dwell time of range 1.725 µs. Fluorophores were excited with a 440 nm laser derived from an 80 MHz pulsed White Light Laser (Leica Microsystems GmbH, Wetzlar, Germany). The fluorophore emission was collected with Hybrid Detectors (HyDS, Leica Microsystems GmbH, Wetzlar, Germany) with a spectral window of 445–650 nm. Two 1 µm × 3 µm regions were selected at the edge of the cell; measurements were calculated from 1 z-slice.

Atomic force microscopy—1 × 10^5 cells MDA-MB-231 cells were plated on rimmed petri dishes (Ted Pella, Inc) coated with 1 mg/mL unlabeled gelatin. The Young's modulus of MDA-MB-231 cells in L15 phenol red free cell culture media (Gibco) with 10% FBS (Gemini Bio) was measured using a Flex-Bio AFM (Nanosurf AG, Switzerland) equipped with an 178 inverted microscope Axio Observer (Carl Zeiss) and an environmental control enclosure. The AFM is operated in static force mode, and with a cantilever with spring constant 0.22 N, and its silicon tip with radius <10 nm (Stat0.2LAuD, Nanosurf AG, Switzerland). Force curves were measured across cells within 30 µm windows with each data point collected every 2 µm. A custom Matlab (MathWorks, Natick, MA, USA) code was written to select and average the elasticity of 25 data points that have the highest contact points with the cell, which corresponds to the nucleus of the cell. The Sneddon model was used to approximate the Young's modulus, with a cone with half angle 15°, fitting from 0 – 500 pN.

Bulk RNAseq of tumors—Flash-frozen tumors (3 Ctrl mice, 3 KD #1 mice) were homogenized using the gentleMACS Octo Dissociator (Miltenyi Biotec), and total RNA was extracted with a RNeasy Mini Kit (Qiagen). RNA purity and concentration were calculated with a NanoDrop™ 2000 (Thermo Scientific), and RNA integrity was analyzed with the Agilent 2100 Bioanalyzer (Agilent). RNA Integrity Numbers (RIN) were calculated per sample: all samples had RIN between 9.0 and 10.0. Novogene conducted the library preparation, RNA sequencing, and analysis. Briefly, mRNA was purified with poly-T oligo-attached magnetic beads, randomly fragmented, and was subjected to cDNA synthesis and library generation using an NEBNext® Ultra™ RNA Library Prep Kit. Library quality was assessed with q-PCR to quantify library effective concentration (>2 nM). The library was diluted to 1.5 ng/mL using Qubit2.0 (Invitrogen) results, and insert size was detected by an Agilent 2100 Bioanalyzer (Agilent). Sequencing was performed with an Illumina NovaSeq 6000 system (Illumina). Raw reads were filtered and mapped with STAR software.

Differential expression analysis of Ctrl and KD #1 groups (three biological replicates per group) was performed using the DESeq2 R package (v2_1.6.3) (Anders and Huber, 2010).

P-values were adjusted using the Benjamini and Hochberg's approach for controlling the False Discovery Rate (FDR), and the threshold of differential gene expression was p_{adj} <

0.05. For KEGG and Reactome pathway enrichment analysis, a clusterProfiler R package (v2.4.3) was used.

Intravital imaging of mice—Mice with tumors <1 cm^3 were anesthetized with 1.5–2% isoflurane with the oxygen flowmeter at 0.8 to 1.5 L/min. A skin-flap surgery was performed to expose the tumor, and a mammary imaging window was placed over the primary tumor. Intravital imaging of NCG mice (Strain Code: 572, Charles River Labs) with MDA-MB-231 GFP tumors was conducted as in (Patsialou et al., 2013) using an Olympus FluoView FV1000MPE multiphoton laser scanning microscope with a 25× NA 1.05 dipping water. The light source is a Ti:Sapphire femtosecond-pulsed laser system (Coherent Chameleon Vision II laser) that is tunable from 680 nm to 1080 nm, as well as a 473 nm laser diode for single photon excitation. Second harmonic generation (SHG) and GFP signal was acquired from 880 nm excitation with a 5 μm z step-size; images were acquired every 2 min for 30 min movies. x-y drift of movies was corrected with HyperStackReg plugin (FIJI (Schindelin et al., 2012), 10.5281/zenodo.2252521), and a TrackMate plugin (FIJI (Schindelin et al., 2012; Tinevez et al., 2017)) was used to track cells.

Two-photon imaging of tissues—Tissues were isolated from NCG mice and imaged immediately with an Olympus FluoView FV1000MPE multiphoton laser scanning microscope using a 25× NA 1.05 dipping water objective. Tissues were excited at 880 nm with a Coherent Chameleon Vision II laser. For tissues expressing H2B-RFP in addition to SHG and GFP, sequential imaging at 880 nm followed by 1000 nm was acquired, and images were aligned with TrakEm2 (FIJI (Cardona et al., 2012; Preibisch et al., 2009)).

Tissue collection, immunofluorescence, and imaging of tissue sections—All tissues were obtained from NOD/SCID/gamma mice (NCG mice, Strain Code: 572, Charles River Labs), fixed overnight in 10% neutral-buffered formalin, and embedded in paraffin. 5 μm serial sections of primary tumors and lungs were used for staining.

5 μm sections of paraffin-embedded tissues were deparaffinized in xylene, dehydrated with a graded series of alcohol, and rehydrated in 1X PBS. Heat-induced antigen retrieval was performed in 10 mM citrate buffer (pH 6.0) in a pressure cooker. After 2–3 h, sections were blocked with 10% donkey serum in 0.5% Tween 20 in 1X PBS for 2 h at room temperature, incubated with primary antibodies in 1% donkey serum in 0.5% Tween 20 in 1X PBS overnight at 4°C, and washed 3 times in 0.5% Tween 20 in 1X PBS. Fluorescently-labeled secondary antibodies (AlexaFluor, Molecular Probes) were added for 2 h at room temperature, and 10 μg/mL DAPI (Biotium) was added at the last wash to label DNA. Coverslips were mounted with Fluoromount-G Mounting Media (Southern Biotech). A Leica TCS SP5 DMI inverted microscope was used for fluorescent imaging of tissue sections (40× NA 1.25, 63X, NA 1.4).

Proteomics analysis of secretome

Secretome sample preparation: Conditioned media from 5 × 10^6 cells was collected after 48 h and concentrated with Amicon Ultra-15 3000 MWCO filters (Millipore). Amicon Ultra-4 3000 MWCO filters (Millipore) were used for buffer exchange to 1X

PBS. Protein concentration was measured with a Pierce™ BCA protein assay (Thermo Fisher), and protein quality was assessed by running 5 μg of protein on a 12% SDS-PAGE gel and stained with Coomassie Brilliant Blue. Proteomics analysis was conducted at the Northwestern Proteomics Core facility. Briefly, 50 μg each protein was concentrated and purified by acetone/tca precipitation and resulting protein pellet was resuspended in 50 μL of 8 M urea in 400 mM ammonium bicarbonate, pH 7.8, reduced with 4 mM dithiothreitol at 50°C for 30 min, and cysteines were alkylated with 18 mM iodoacetamide in the dark for 30 min. The solution was then diluted to <2 M urea (final concentration) and trypsin (Promega, Madison, WI) was added at final trypsin/protein ratio of 1:50 prior to overnight incubation at 37°C with shaking. The resulting peptides were desalted using solid phase extraction on a Pierce C18 Spin column and eluted in 80 μL of 80% acetonitrile in 0.1% formic acid. After lyophilization, peptides were reconstituted with 5% acetonitrile in 0.1% formic acid. Three biological replicates and two technical duplicates were run for each condition.

Liquid chromatography tandem mass spectrometry (LC-MS/MS) data acquisition and processing—Peptides were analyzed by LC-MS/MS using a Dionex UltiMate 3000 Rapid Separation nanoLC and a Q Exactive™ HF Hybrid Quadrupole-Orbitrap™ Mass Spectrometer (Thermo Fisher Scientific Inc, San Jose, CA). Approximately 2 μg of peptide samples was loaded onto the trap column, which was 150 μm × 3 cm in-house packed C18 beads. The analytical column was a 75 μm × 10.5 cm PicoChip column packed with 3 μm C18 beads (New Objective, Inc. Woburn, MA). The flow rate was kept at 300 nL/min. Solvent A was 0.1% FA in water and Solvent B was 0.1% FA in ACN. The peptide was separated on a 120-min analytical gradient from 5% ACN/0.1% FA to 40% ACN/0.1% FA. The mass spectrometer was operated in data-dependent mode. The source voltage was 2.40 kV. MS^1 scans were acquired from 300 to 2000 *m/z* at 60,000 resolving power and automatic gain control (AGC) set to 3×10^6. The top 20 most abundant precursor ions in each MS^1 scan were selected for fragmentation. Precursors were selected with an isolation width of 2 *m/z* and fragmented by Higher-energy collisional dissociation (HCD) at 30% normalized collision energy in the HCD cell. Previously selected ions were dynamically excluded from re-selection for 20 s. The MS^2 minimum AGC was set to 1×10^3. Data was acquired in technical duplicates.

Data analysis—Proteins were identified from the tandem mass spectra extracted by Xcalibur version 4.0. MS/MS spectra were searched against the SwissProt *Homo sapiens* database using Mascot search engine (Matrix Science, London, UK; version 2.7.0). All searches included carbamidomethyl cysteine as a fixed modification and oxidized Lys, Pro, and Met; deamidated Asn and Gln; and acetylated N-term as variable modifications. Three missed tryptic cleavages were allowed. The MS^1 precursor mass tolerance was set to 10 ppm and the MS^2 tolerance was set to 0.05 Da. The search result was visualized by Scaffold v 5.0(Proteome Software, INC., Portland, OR). A 1% false discovery rate cutoff was applied at the peptide level. Only proteins with a minimum of two unique peptides above the cutoff were considered for further study. Raw mass spectrometry data will be made available upon publication and via request to the authors. The mass spectrometry proteomics data have been deposited to the ProteomeXchange Consortium via the PRIDE (Perez-Riverol et al., 2019)

partner repository with the dataset identifier PXD026102 and 10.6019/PXD026102 and will be made publicly available upon acceptance of the manuscript.

Luminex assays—Conditioned media from cells and concentrated with Amicon Ultra-4 3000 MWCO filters (Millipore). TGF-β Luminex assays were performed by Eve Technologies (Calgary, Alberta) using a TGF-β 3-Plex Cytokine Array. Samples were run in duplicate. Regression analysis is performed as a function of the software analyser. Bio-Plex Manager™ software regression equations use the Expected Concentration values of the standard, as defined in the manufacturer's Instructions for Use (IFU), and Fluorescence Intensity (FI) to generate the Observed Concentration.

Apoptosis assays—An APC Annexin V detection kit with 7-AAD (BioLegend) was used to determine apoptosis and necrosis. Briefly, 5 × 10^6 cells were collected per sample, washed, and resuspended in 100 μL of binding buffer. 7-AAD viability solution and FITC-annexin V were added to the samples, vortexed and incubated at room temperature for 15 min, and an additional 400 μL of binding buffer was added to each sample. FACS was done on the BD LSRFortessa and analyzed using FlowJo v.10. At least 1 × 10^5 cells per sample was recorded; data is in triplicate and represented as mean +/SEM.

Cell cycle analysis and pyronin Y staining—500,000 cells were incubated with 1 μg/mL of Hoechst 33342 solution (BD Biosciences) for 45 min at 37°C, and then incubated for an additional 15 min with 1 μg/mL Pyronin Y (Sigma Aldrich). Samples were analyzed by flow cytometry (BD LSRFortessa). At least 50,000–100,000 data were cells were recorded per sample and analyzed using FlowJo v.10.

QUANTIFICATION AND STATISTICAL ANALYSIS

Statistical analyses were performed with GraphPad PRISM 9.0.1, or using R-packages as explained in the Methods. Statistical tests used to analyze data are listed in the figure legends, and exact values of n and p values are either listed in the figure legends or displayed in figures. All data, unless otherwise specified, was analyzed by non-parametric tests. Normality was assessed using GraphPad PRISM 9.0.1. Differences were considered significant if $p < 0.05$, or $p_{adj} < 0.05$, depending on the experiment. Sample size was determined empirically.

Supplementary Material

Refer to Web version on PubMed Central for supplementary material.

ACKNOWLEDGMENTS

We would like to thank Young Ah Goo and Shilpa Dilip Kumar for expert advice and services. Multiphoton microscopy was performed in the Microscopy CoRE at the Icahn School of Medicine at Mount Sinai and was supported by (1S10RR026639). We acknowledge the Microscopy Core and the Flow Cytometry Core from Mount Sinai. We want to thank Ni-Ka Ford for her illustrations. We thank the Aguirre-Ghiso and Sosa laboratories for helpful discussions. We thank Jared A. Rouchard, Colin Morrow, Melanie Freeman, David Parks, Angela Willis, Matthew Grant, and Jenny Hagemeier at the HHMI Janelia Research Campus for zebrafish care and cell culture maintenance. Proteomics services were performed by the Northwestern Proteomics Core Facility, generously supported by NCI CCSG P30 CA060553 awarded to the Robert H. Lurie Comprehensive Cancer Center, instrumentation award (S10OD025194) from NIH Office of Director, and the National Resource for

Translational and Developmental Proteomics supported by P41 GM108569. C.M. received support from an NIH T32 CA078207 Training Program in Cancer Biology. This work was supported by an NCI Career Transition Award (K22CA196750), an NCI R01 (CA244780) (to J.J.B.-C.), a Damon Runyon-Rachleff Innovation Award (DDR-47-17 to B.L.M. and D.Q.M), a Stony Brook-Mount Sinai pilot award (to J.J.B.-C., B.L.M., and D.Q.M.) the Pershing Square Sohn Cancer Research Alliance (B.L.M.), and the Tisch Cancer Institute NIH Cancer Center grant (P30 CA196521).

REFERENCES

Aguirre-Ghiso JA (2007). Models, mechanisms and clinical evidence for cancer dormancy. Nat. Rev. Cancer 7, 834–846. 10.1038/nrc2256. [PubMed: 17957189]

Aguirre-Ghiso JA, and Sosa MS (2018). Emerging topics on disseminated cancer cell dormancy and the paradigm of metastasis. Annu. Rev. Cell Biol. 2, 377–393. 10.1146/annurev-cancerbio-030617-050446.

Anders S, and Huber W (2010). Differential expression analysis for sequence count data. Genome Biol. 11, R106, Epub 2010 Oct 27. 10.1186/gb-2010-11-10-r106. [PubMed: 20979621]

Arismendi-Morillo G, Hoa NT, Ge L, and Jadus MR (2012). Mitochondrial network in glioma's invadopodia displays an activated state both in situ and in vitro: potential functional implications. Ultrastruct. Pathol. 36, 409–414. 10.3109/01913123.2012.694582. [PubMed: 23216239]

Arozarena I, and Wellbrock C (2019). Phenotype plasticity as enabler of melanoma progression and therapy resistance. Nat. Rev. Cancer 19, 377–391. 10.1038/s41568-019-0154-4. [PubMed: 31209265]

Bayarmagnai B, Perrin L, Esmaeili Pourfarhangi K, Graña X, Tüzel E, and Gligorijevic B (2019). Invadopodia-mediated ECM degradation is enhanced in the G1 phase of the cell cycle. J. Cell Sci. 132, jcs227116. 10.1242/jcs.227116. [PubMed: 31533971]

Beaty BT, and Condeelis J (2014). Digging a little deeper: the stages of invadopodium formation and maturation. Eur. J. Cell Biol. 93, 438–444. 10.1016/j.ejcb.2014.07.003. [PubMed: 25113547]

Bragado P, Estrada Y, Parikh F, Krause S, Capobianco C, Farina HG, Schewe DM, and Aguirre-Ghiso JA (2013). TGF-β2 dictates disseminated tumour cell fate in target organs through TGF-β-RIII and p38α/β signalling. Nat. Cell Biol. 15, 1351–1361. 10.1038/ncb2861. [PubMed: 24161934]

Bravo-Cordero JJ, Oser M, Chen X, Eddy R, Hodgson L, and Condeelis J (2011). A novel spatiotemporal RhoC activation pathway locally regulates cofilin activity at invadopodia. Curr. Biol. 21, 635–644. 10.1016/j.cub.2011.03.039. [PubMed: 21474314]

Cardona A, Saalfeld S, Schindelin J, Arganda-Carreras I, Preibisch S, Longair M, Tomancak P, Hartenstein V, and Douglas RJ (2012). TrakEM2 software for neural circuit reconstruction. PLoS One 7, e38011. 10.1371/journal.pone.0038011. [PubMed: 22723842]

Condeelis J, and Segall JE (2003). Intravital imaging of cell movement in tumours. Nat. Rev. Cancer 3, 921–930. 10.1038/nrc1231. [PubMed: 14737122]

Derynck R, and Budi EH (2019). Specificity, versatility, and control of TGF-β family signaling. Sci. Signal. 12, eaav5183. 10.1126/scisignal.aav5183.

Ding C, Li Y, Xing C, Zhang H, Wang S, and Dai M (2020). Research progress on slit/robo pathway in pancreatic cancer: emerging and promising. JAMA Oncol. 2020, 2845906. 10.1155/2020/2845906.

Eddy RJ, Weidmann MD, Sharma VP, and Condeelis JS (2017). Tumor cell invadopodia: invasive protrusions that orchestrate metastasis. Trends Cell Biol. 27, 595–607. 10.1016/j.tcb.2017.03.003. [PubMed: 28412099]

Feng Y, Feng L, Yu D, Zou J, and Huang Z (2016). srGAP1 mediates the migration inhibition effect of Slit2-Robo1 in colorectal cancer, pp. 1–10. 10.1186/s13046-016-0469-x.

Follain G, Osmani N, Azevedo AS, Allio G, Mercier L, Karreman MA, Solecki G, Garcia Leòn MJ, Lefebvre O, Fekonja N, et al. (2018). Hemodynamic forces tune the arrest, adhesion, and extravasation of circulating tumor cells. Dev. Cell 45, 33–52.e12. 10.1016/j.devcel.2018.02.015. [PubMed: 29634935]

Friedl P, and Alexander S (2011). Cancer invasion and the microenvironment: plasticity and reciprocity. Cell 147, 992–1009. 10.1016/j.cell.2011.11.016. [PubMed: 22118458]

Friedl P, and Wolf K (2003). Tumour-cell invasion and migration: diversity and escape mechanisms. Nat. Rev. Cancer 3, 362–374. [PubMed: 12724734]

Gil-Henn H, Patsialou A, Wang Y, Warren MS, Condeelis JS, and Koleske AJ (2013). Arg/Abl2 promotes invasion and attenuates proliferation of breast cancer in vivo. Oncogene 32, 2622–2630. 10.1038/onc.2012.284. [PubMed: 22777352]

Gligorijevic B, Wyckoff J, Yamaguchi H, Wang Y, Roussos ET, and Condeelis J (2012). N-WASP-mediated invadopodium formation is involved in intravasation and lung metastasis of mammary tumors. J. Cell Sci. 125, 724–734. 10.1242/jcs.092726. [PubMed: 22389406]

Haga RB, and Ridley AJ (2016). Rho GTPases: regulation and roles in cancer cell biology. Small GTPases 7, 207–221. 10.1080/21541248.2016.1232583. [PubMed: 27628050]

Hagedorn EJ, and Sherwood DR (2011). Cell invasion through basement membrane: the anchor cell breaches the barrier. Curr. Opin. Cell Biol. 23, 589–596. 10.1016/j.ceb.2011.05.002. [PubMed: 21632231]

Han YL, Pegoraro AF, Li H, Li K, Yuan Y, Xu G, Gu Z, Sun J, Hao Y, Gupta SK, et al. (2020). Cell swelling, softening and invasion in a three-dimensional breast cancer model. Nat. Phys. 16, 101–108. 10.1038/s41567-019-0680-8. [PubMed: 32905405]

Hanna S, Miskolci V, Cox D, and Hodgson L (2014). A new genetically encoded single-chain biosensor for Cdc42 based on FRET, useful for live-cell imaging. PLoS One 9, e96469. 10.1371/journal.pone.0096469. [PubMed: 24798463]

Harney AS, Arwert EN, Entenberg D, Wang Y, Guo P, Qian BZ, Oktay MH, Pollard JW, Jones JG, and Condeelis JS (2015). Real-time imaging reveals local, transient vascular permeability, and tumor cell intravasation stimulated by $TIE2^{hi}$ macrophage–derived VEGFA. Cancer Discov. 5, 932–943. 10.1158/2159-8290.CD-15-0012. [PubMed: 26269515]

He H, Bronisz A, Liyanarachchi S, Nagy R, Li W, Huang Y, Akagi K, Saji M, Kula D, Wojcicka A, et al. (2013). SRGAP1 is a candidate gene for papillary thyroid carcinoma susceptibility. J. Clin. Endocrinol. Metab. 98, E973–E980. 10.1210/jc.2012-3823. [PubMed: 23539728]

Hoek KS, Eichhoff OM, Schlegel NC, Döbbeling U, Kobert N, Schaerer L, Hemmi S, and Dummer R (2008). In vivo switching of human melanoma cells between proliferative and invasive states. Cancer Res. 68, 650–656. 10.1158/0008-5472.CAN-07-2491. [PubMed: 18245463]

Huang T, Zhou Y, Zhang J, Wong CC, Li W, Kwan JSH, Yang R, Chan AKY, Dong Y, Wu F, et al. (2018). SRGAP1, a crucial target of miR-340 and miR-124, functions as a potential oncogene in gastric tumorigenesis. Oncogene 37, 1159–1174. 10.1038/s41388-017-0029-7. [PubMed: 29234151]

Jiang WG, Sanders AJ, Katoh M, Ungefroren H, Gieseler F, Prince M, Thompson SK, Zollo M, Spano D, Dhawan P, et al. (2015). Tissue invasion and metastasis: molecular, biological and clinical perspectives. Semin. Cancer Biol. 35, S244–S275. 10.1016/j.semcancer.2015.03.008. [PubMed: 25865774]

Jordan NV, Chen K, Guerrier S, Coutinho-budd J, and Sassa T (2009). The F-BAR domain of srGAP2 induces membrane protrusions required for neuronal migration and morphogenesis. Cell 138, 990–1004. 10.1016/j.cell.2009.06.047. [PubMed: 19737524]

Juin A, Di Martino J, Leitinger B, Henriet E, Gary A-S, Paysan L, Bomo J, Baffet G, Gauthier-Rouvière C, Rosenbaum J, et al. (2014). Discoidin domain receptor 1 controls linear invadosome formation via a Cdc42-Tuba pathway. J. Cell Biol. 207, 517–533. 10.1083/jcb.201404079. [PubMed: 25422375]

Kelley LC, Chi Q, Cáceres R, Hastie E, Schindler AJ, Jiang Y, Matus DQ, Plastino J, and Sherwood DR (2019). Adaptive F-actin polymerization and localized ATP production drive basement membrane invasion in the absence of MMPs. Dev. Cell 48, 313–328.e8. 10.1016/j.devcel.2018.12.018. [PubMed: 30686527]

Kohrman AQ, and Matus DQ (2017). Divide or conquer: cell cycle regulation of invasive behavior. Trends Cell Biol. 27, 12–25. 10.1016/j.tcb.2016.08.003. [PubMed: 27634432]

KOO S, MARTIN G, and TOUSSAINT LG (2015). MicroRNA-145 promotes the phenotype of human glioblastoma cells selected for invasion. Anticancer Res. 35, 3209–3215. [PubMed: 26026080]

Lahoz A, and Hall A (2012). A tumor suppressor role for srGAP3 in mammary epithelial cells. Oncogene 32, 4854–4860. 10.1038/onc.2012.489. [PubMed: 23108406]

Lambert AW, Pattabiraman DR, and Weinberg RA (2017). Emerging biological principles of metastasis. Cell 168, 670–691. 10.1016/j.cell.2016.11.037. [PubMed: 28187288]

Lekka M, Gil D, Pogoda K, Dulinska-Litewka J, Jach R, Gostek J, Kly-menko O, Prauzner-Bechcicki S, Stachura Z, Wiltowska-Zuber J, et al. (2012). Cancer cell detection in tissue sections using AFM. Arch. Biochem. Biophys. 518, 151–156. 10.1016/j.abb.2011.12.013. [PubMed: 22209753]

Leong HS, Robertson AE, Stoletov K, Leith SJ, Chin CA, Chien AE, Hague MN, Ablack A, Carmine-Simmen K, McPherson VA, et al. (2014). Invadopodia are required for cancer cell Extravasation and are a therapeutic target for metastasis. Cell Rep. 8, 1558–1570. 10.1016/j.celrep.2014.07.050. [PubMed: 25176655]

Liu TL, Upadhyayula S, Milkie DE, Singh V, Wang K, Swinburne IA, Mosaliganti KR, Collins ZM, Hiscock TW, Shea J, et al. (2018). Observing the cell in its native state: imaging subcellular dynamics in multicellular organisms. Science, eaaq1392. 10.1126/science.aaq1392. [PubMed: 29674564]

Logotheti S, Marquardt S, Richter C, Sophie Hain R, Murr N, Takan I, Pavlopoulou A, and Pützer BM (2020). Neural networks recapitulation by cancer cells promotes disease progression: a novel role of p73 isoforms in cancer-neuronal crosstalk. Cancers 12, E3789. 10.3390/cancers12123789. [PubMed: 33339112]

Lohmer LL, Kelley LC, Hagedorn EJ, and Sherwood DR (2014). Invadopodia and basement membrane invasion in vivo. Cell Adhes. Migrat. 8, 246–255. 10.4161/cam.28406.

Marko TA, Shamsan GA, Edwards EN, Hazelton PE, Rathe SK, Cornax I, Overn PR, Varshney J, Diessner BJ, Moriarity BS, et al. (2016). Slit-Robo GTPase-Activating Protein 2 as a metastasis suppressor in osteosarcoma. Sci. Rep. 6, 39059–39111. 10.1038/srep39059. [PubMed: 27966608]

Di Martino J, Henriet E, Ezzoukhry Z, Mondal C, Bravo-Cordero JJ, Moreau V, and Saltel F (2017). 2D and 3D matrices to study linear invadosome formation and activity. JoVE 2017. 10.3791/54911.

Matus DQ, Lohmer LL, Kelley LC, Schindler AJ, Kohrman AQ, Barkoulas M, Zhang W, Chi Q, and Sherwood DR (2015). Invasive cell fate requires G1 cell-cycle arrest and histone deacetylase-mediated changes in gene expression. Dev. Cell 35, 162–174. 10.1016/j.devcel.2015.10.002. [PubMed: 26506306]

Mehlen P, Delloye-bourgeois C, and Chédotal A (2011). Novel roles for Slits and netrins : axon guidance cues as anticancer targets?, pp. 1–10. 10.1038/nrc3005.

Miskolci V, Wu B, Moshfegh Y, Cox D, and Hodgson L (2016). Optical tools to study the isoform-specific roles of small GTPases in immune cells. J. Immunol. 196, 3479–3493. 10.4049/jimmunol.1501655. [PubMed: 26951800]

Mondal C, Di Martino S, J., and Bravo-Cordero JJ (2020). Actin Dynamics during Tumor Cell Dissemination (Academic Press).

Murphy DA, and Courtneidge SA (2011). The “ins” and “outs” of podosomes and invadopodia: characteristics, formation and function. Nat. Rev. Mol. Cell Biol. 12, 413–426. 10.1038/nrm3141. [PubMed: 21697900]

Nobre AR, Risson E, Singh DK, Di Martino JS, Cheung JF, Wang J, Johnson J, Russnes HG, Bravo-Cordero JJ, Birbrair A, et al. (2021). Bone marrow NG2+/Nestin+ mesenchymal stem cells drive DTC dormancy via TGF-β2. Nat. Cancer 2, 327–339. 10.1038/s43018-021-00179-8. [PubMed: 34993493]

Obenauf AC, and Massagué J (2015). Surviving at a distance: organ-specific metastasis. Trends Cancer 1, 76–91. 10.1016/j.trecan.2015.07.009. [PubMed: 28741564]

O’Connell MP, and Weeraratna AT (2013). Change is in the air: the hypoxic induction of phenotype switching in melanoma. J. Invest. Dermatol. 133, 2316–2317. 10.1038/jid.2013.208. [PubMed: 24030649]

Olmeda D, Cerezo-Wallis D, Riveiro-Falkenbach E, Pennacchi PC, Contreras-Alcalde M, Ibarz N, Cifdaloz M, Catena X, Calvo TG, Cañón E, et al. (2017). Whole-body imaging of lymphovascular niches identifies premetastatic roles of midkine. Nature 546, 676–680. 10.1038/nature22977. [PubMed: 28658220]

Oser M, Yamaguchi H, Mader CC, Bravo-Cordero JJ, Arias M, Chen X, Desmarais V, van Rheenen J, Koleske AJ, and Condeelis J (2009). Cortactin regulates cofilin and N-WASp activities to control the stages of invadopodium assembly and maturation. J. Cell Biol. 186, 571–587. 10.1083/jcb.200812176. [PubMed: 19704022]

Patsialou A, Wang Y, Lin J, Whitney K, Goswami S, Kenny PA, and Condeelis JS (2012). Selective gene-expression profiling of migratory tumor cells in vivo predicts clinical outcome in breast cancer patients. Breast Cancer Res. 14, R139. 10.1186/bcr3344. [PubMed: 23113900]

Patsialou A, Bravo-Cordero JJ, Wang Y, Entenberg D, Liu H, Clarke M, and Condeelis JS (2013). Intravital multiphoton imaging reveals multicellular streaming as a crucial component of in vivo cell migration in human breast tumors. IntraVital 2, e25294. 10.4161/intv.25294. [PubMed: 25013744]

Perez-Riverol Y, Csordas A, Bai J, Bernal-Llinares M, Hewapathirana S, Kundu DJ, Inuganti A, Griss J, Mayer G, Eisenacher M, et al. (2019). The PRIDE database and related tools and resources in 2019: improving support for quantification data. Nucleic Acids Res. 47, D442–D450. 10.1093/nar/gky1106. [PubMed: 30395289]

Pertz O, Hodgson L, Klemke RL, and Hahn KM (2006). Spatiotemporal dynamics of RhoA activity in migrating cells. Nature 440, 1069–1072. [PubMed: 16547516]

Pignatelli J, Tumbarello DA, Schmidt RP, and Turner CE (2012). Hic-5 promotes invadopodia formation and invasion during TGF-β-induced epithelial-mesenchymal transition. J. Cell Biol. 197, 421–437. 10.1083/jcb.201108143. [PubMed: 22529104]

Preibisch S, Saalfeld S, and Tomancak P (2009). Globally optimal stitching of tiled 3D microscopic image acquisitions. Bioinformatics 25, 1463–1465. 10.1093/bioinformatics/btp184. [PubMed: 19346324]

Prunier C, Baker D, Ten Dijke P, and Ritsma L (2019). TGF-B family signaling pathways in cellular dormancy. Trends Cancer 5, 66–78. 10.1016/j.trecan.2018.10.010. [PubMed: 30616757]

Roh-Johnson M, Bravo-Cordero JJ, Patsialou A, Sharma VP, Guo P, Liu H, Hodgson L, and Condeelis J (2014). Macrophage contact induces RhoA GTPase signaling to trigger tumor cell intravasation. Oncogene 33, 4203–4212. 10.1038/onc.2013.377. [PubMed: 24056963]

Schindelin J, Arganda-Carreras I, Frise E, Kaynig V, Longair M, Pietzsch T, Preibisch S, Rueden C, Saalfeld S, Schmid B, et al. (2012). Fiji: an open-source platform for biological-image analysis. Nat. Methods 9, 676–682. 10.1038/nmeth.2019. [PubMed: 22743772]

Sharma S, Santiskulvong C, Rao J, Gimzewski JK, and Dorigo O (2014). The role of Rho GTPase in cell stiffness and cisplatin resistance in ovarian cancer cells. Integr. Biol. 6, 611–617. 10.1039/c3ib40246k.

Sharma VP, Entenberg D, and Condeelis J (2013). High-resolution live-cell imaging and time-lapse microscopy of invadopodium dynamics and tracking analysis. Methods Mol. Biol. 1046, 343–357. 10.1007/978-1-62703-538-5_21. [PubMed: 23868599]

Sherwood DR, and Sternberg PW (2003). Anchor cell invasion into the vulval epithelium in C. elegans. Dev. Cell 5, 21–31. 10.1016/s1534-5807(03)00168-0. [PubMed: 12852849]

Sosa MS, Bragado P, and Aguirre-Ghiso JA (2014). Mechanisms of disseminated cancer cell dormancy: an awakening field. Nat. Rev. Cancer 14, 611–622. 10.1038/nrc3793. [PubMed: 25118602]

Spencer SL, Cappell SD, Tsai FC, Overton KW, Wang CL, and Meyer T (2013). XThe proliferation-quiescence decision is controlled by a bifurcation in CDK2 activity at mitotic exit. Cell 155, 369–383. 10.1016/j.cell.2013.08.062. [PubMed: 24075009]

Spuul P, Ciufici P, Veillat V, Leclercq A, Daubon T, Kramer IJ, and Génot E (2014). Importance of RhoGTPases in formation, characteristics, and functions of invadosomes. Small GTPases 5, e28195. 10.4161/sgtp.28713.

Strilic B, and Offermanns S (2017). Intravascular survival and extravasation of tumor cells. Cancer Cell 32, 282–293. 10.1016/j.ccell.2017.07.001. [PubMed: 28898694]

Stylli SS, Stacey TTI, Verhagen AM, Xu SS, Pass I, Courtneidge SA, and Lock P (2009). Nck adaptor proteins link Tks5 to invadopodia actin regulation and ECM degradation. J. Cell Sci. 122, 2727–2740. 10.1242/jcs.046680. [PubMed: 19596797]

Tinevez J-Y, Perry N, Schindelin J, Hoopes GM, Reynolds GD, Laplantine E, Bednarek SY, Shorte SL, and Eliceiri KW (2017). TrackMate: an open and extensible platform for single-particle tracking. Methods 115, 80–90. 10.1016/j.ymeth.2016.09.016. [PubMed: 27713081]

Wagh AA, Roan E, Chapman KE, Desai LP, Rendon DA, Eckstein EC, and Waters CM (2008). Localized elasticity measured in epithelial cells migrating at a wound edge using atomic force

microscopy. Am. J. Physiol. Lung Cell Mol. Physiol. 295, L54–L60. 10.1152/ajplung.00475.2007. [PubMed: 18487359]

Widmer DS, Hoek KS, Cheng PF, Eichhoff OM, Biedermann T, Raaijmakers MIG, Hemmi S, Dummer R, and Levesque MP (2013). Hypoxia contributes to melanoma heterogeneity by triggering HIF1α-dependent phenotype switching. J. Invest. Dermatol. 133, 2436–2443. 10.1038/jid.2013.115. [PubMed: 23474946]

Williams KC, Cepeda MA, Javed S, Searle K, Parkins KM, Makela AV, Hamilton AM, Soukhtehzari S, Kim Y, Tuck AB, et al. (2019). Invadopodia are chemosensing protrusions that guide cancer cell extravasation to promote brain tropism in metastasis. Oncogene 38, 3598–3615. 10.1038/s41388-018-0667-4. [PubMed: 30651600]

Wong K, Ren XR, Huang YZ, Xie Y, Liu G, Saito H, Tang H, Wen L, Brady-kalnay SM, Mei L, et al. (2001). Signal transduction in neuronal migration : roles of GTPase activating proteins and the small GTPase Cdc42 in the slit-robo pathway. Cell 107, 209–221. [PubMed: 11672528]

Highlights

- BC cells can form actin-rich protrusions during extravasation
- srGAP1 loss promotes invasion and extravasation while reducing metastatic outgrowth
- srGAP1^{low} cells can remain as solitary cells in the lungs of mice with BC tumors
- srGAP1 mediates a proliferative-to-invasive switch dependent on TGF-β2 signaling

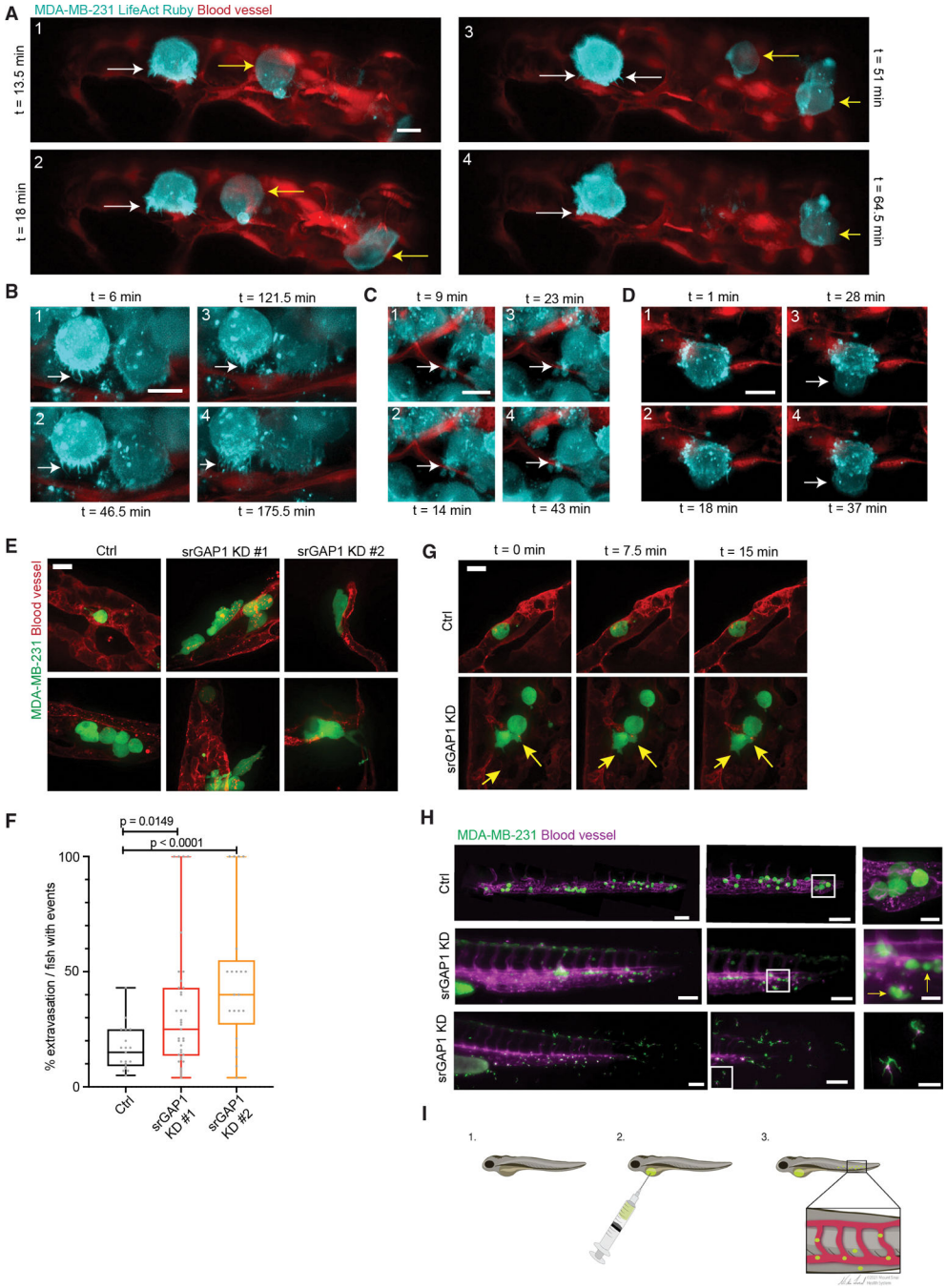

Figure 1. Breast cancer cells form protrusive structures during extravasation

(A–D) Lattice light-sheet microscopy of MDA-MB-231 cells expressing LifeAct Ruby injected intravenously in zebrafish xenografts. Yellow arrows point toward rolling BC cells in the blood. White arrows point to: (A and B) protrusions toward endothelium; (C) protrusions into the endothelium; (D) protrusions formed by tumor cell after extravasation. Scale bar, 10 μm. Time in min.

(E) Representative images of Ctrl, srGAP1 KD #1, and srGAP1 KD #2 MDA-MB-231-GFP cells injected into Tg(kdrl:RFP) zebrafish embryos and imaged 24 h post injection (hpi). Scale bar, 20 μm.

(F) Percent of extravasated MDA-MB-231 cells from zebrafish with extravasation events. n = 19 (Ctrl), 37 (srGAP KD #1), and 21 (srGAP1 KD #2) zebrafish. Mann Whitney U test, two-tailed. Data represented as a box and whisker plot, with median and interquartile range in the box and min and max as whiskers.

(G) Time-lapse images of MDA-MB-231 Ctrl and srGAP1 KD #1 cells in zebrafish vasculature. Yellow arrows point to protrusive structures. Scale bar, 20 μm.

(H) Tiled images showing extravasation events at the tailbud of fish. MDA-MB-231 cells. (Top) Ctrl cells imaged 24 h post injection (hpi). (Middle) srGAP KD #1 cells imaged 20 hpi; (bottom) srGAP KD #1 cells imaged 24 hpi. Three representative fish tails shown. Scale bar, 100 μm (left and middle panels), 25 μm (right).

(I) Schematic of zebrafish xenograft setup.

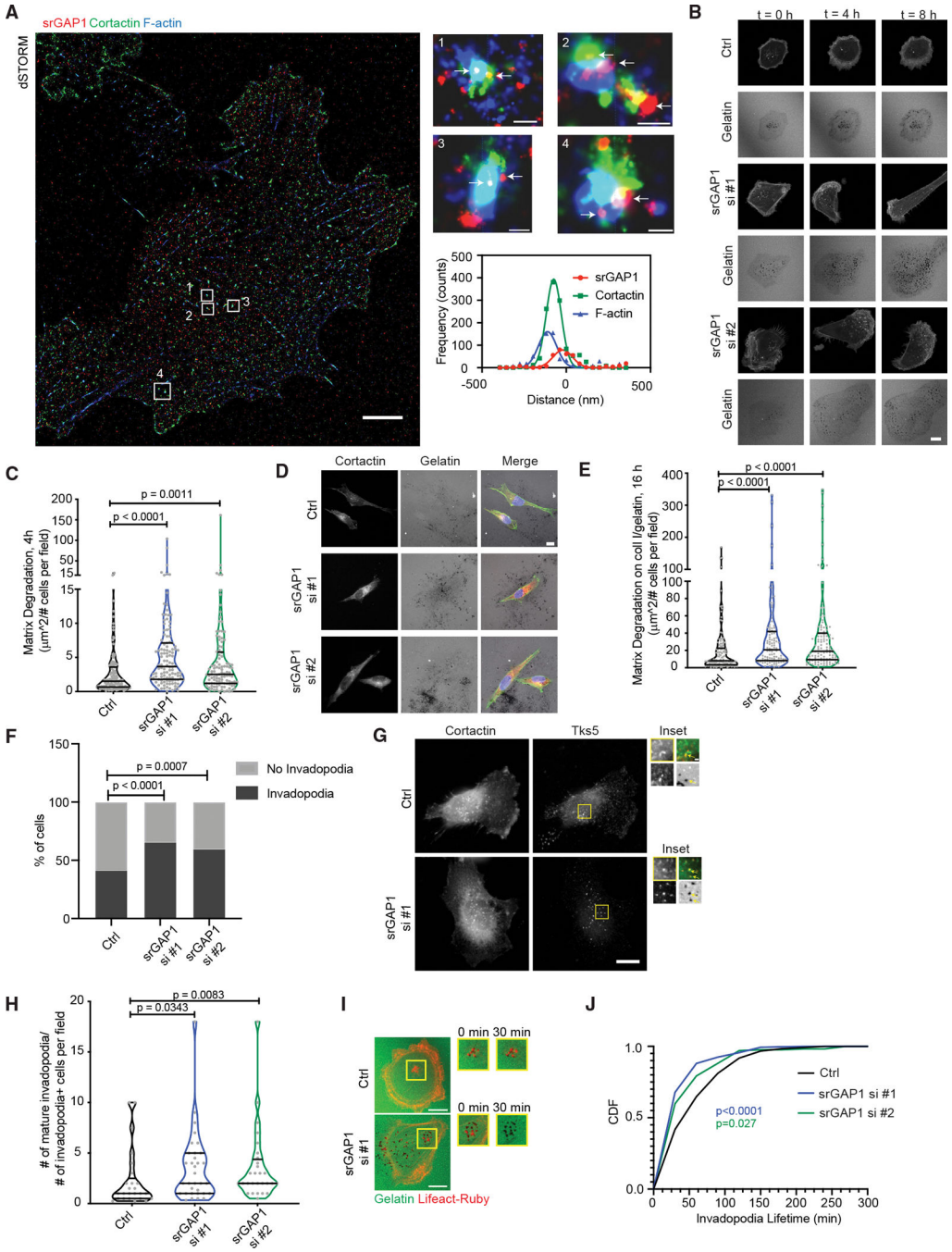

Figure 2. srGAP1 depletion increases matrix degradation by forming more mature invadopodia

(A) Immunofluorescence demonstrating srGAP1, cortactin, and F-actin localization at invadopodia structures using direct STORM of MDA-MB-231 cells. Individual invadopodia noted by numbers and white boxes; arrows point to srGAP1 staining. Scale bars, 5 μm (for cell), 100 nm (for invadopodia #1, 4), 200 nm (for invadopodia #2, 3). For invadopodia #1, respective curve fitting of a region through invadopodia (bottom right).

(B) Time-lapse images of control (Ctrl) or srGAP1 knockdown Lifeact-Ruby MDA-MB-231 cells using siRNAs (srGAP si #1, srGAP1 si #2) and respective matrix degradation on gelatin at 0, 4, and 8 h. Scale bar, 10 μm.

(C) Matrix degradation of Ctrl, srGAP1 si #1, and srGAP1 si #2 MDA-MB-231 cells. Cells plated on fluorescent gelatin for 4 h. n = 114 (Ctrl), 116 (srGAP1 si #1), and 109 (srGAP1 si #2) fields quantified. Data from three independent experiments and represented as a violin plot, horizontal lines are median and interquartile range. Mann-Whitney U test, two-tailed.

(D) Representative images of Ctrl, srGAP1 si #1, and srGAP1 si #2 MDA-MB-231 cells plated on fibrillar collagen I overlaid on fluorescent gelatin for 16 h. Left: cortactin; middle: gelatin matrix; right: cortactin (red)-, F-actin (green)-, DAPI (blue)-labeled tumor cells on the matrix. Scale bar, 10 μm.

(E) Matrix degradation of Ctrl, srGAP1 si #1, and srGAP1 si #2 MDA-MB-231 cells plated on fibrillar collagen I overlaid on fluorescent gelatin for 16 h. n = 119 (Ctrl), 101 (srGAP1 si #1), and 113 (srGAP1 si #2) fields quantified. Data are from three independent experiments and represented as a violin plot; horizontal lines are median and interquartile range. Mann-Whitney U test, two-tailed.

(F) Percent of Ctrl, srGAP1 si #1, and srGAP1 si #2 MDA-MB-231 cells with or without invadopodia at 4 h. n = 226 cells from 64 fields (Ctrl), 166 cells from 73 fields (srGAP1 si #1), 147 cells from 72 fields (srGAP1 si #2) pooled over three independent experiments. Chi-squared test.

(G) Representative images of Ctrl and srGAP1 si #1 MDA-MB-231 cells on gelatin for 4 h. Left: cortactin; right: Tks5 staining. Scale bar, 10 μm. Inset scale bar, 1 μm. Top left: cortactin; bottom left: Tks5; bottom right: gelatin, Top right: merge of cortactin and Tks5. Mature invadopodia are labeled with cortactin and Tks5; black spots on gelatin matrix represent matrix degradation (yellow arrows point to colocalization of invadopodia and matrix degradation).

(H) Number of mature invadopodia of Ctrl, srGAP1 si #1, and srGAP1 si #2 MDA-MB-231 cells at 4 h, n = 25 (Ctrl), n = 33 (srGAP1 si #1), n = 28 (srGAP1 si #2) fields. Data are from three independent experiments and represented as a violin plot; horizontal lines are median and interquartile range. Mann-Whitney U test, two-tailed.

(I) Time-lapse images of invadopodia lifetime at 0 and 30 min. (Left) Lifeact-Ruby Ctrl and srGAP1 si #1 MDA-MB-231 cells on fluorescent gelatin at 0 min. Scale bar, 20 μm. Right panel: insets of mature invadopodia (red fluorescent puncta overlaid on black degradation spots) over time (0 and 30 min).

(J) Cumulative distribution of invadopodia lifetimes of Ctrl, srGAP1 si #1, and srGAP1 si #2 MDA-MB-231 cells. n = 122 invadopodia from 10 cells (Ctrl), 317 invadopodia from 11 cells (srGAP1 si #1), and 169 invadopodia from 11 (srGAP1 si #2) cells. Data from three independent experiments. Kolmogorov-Smirnov test.

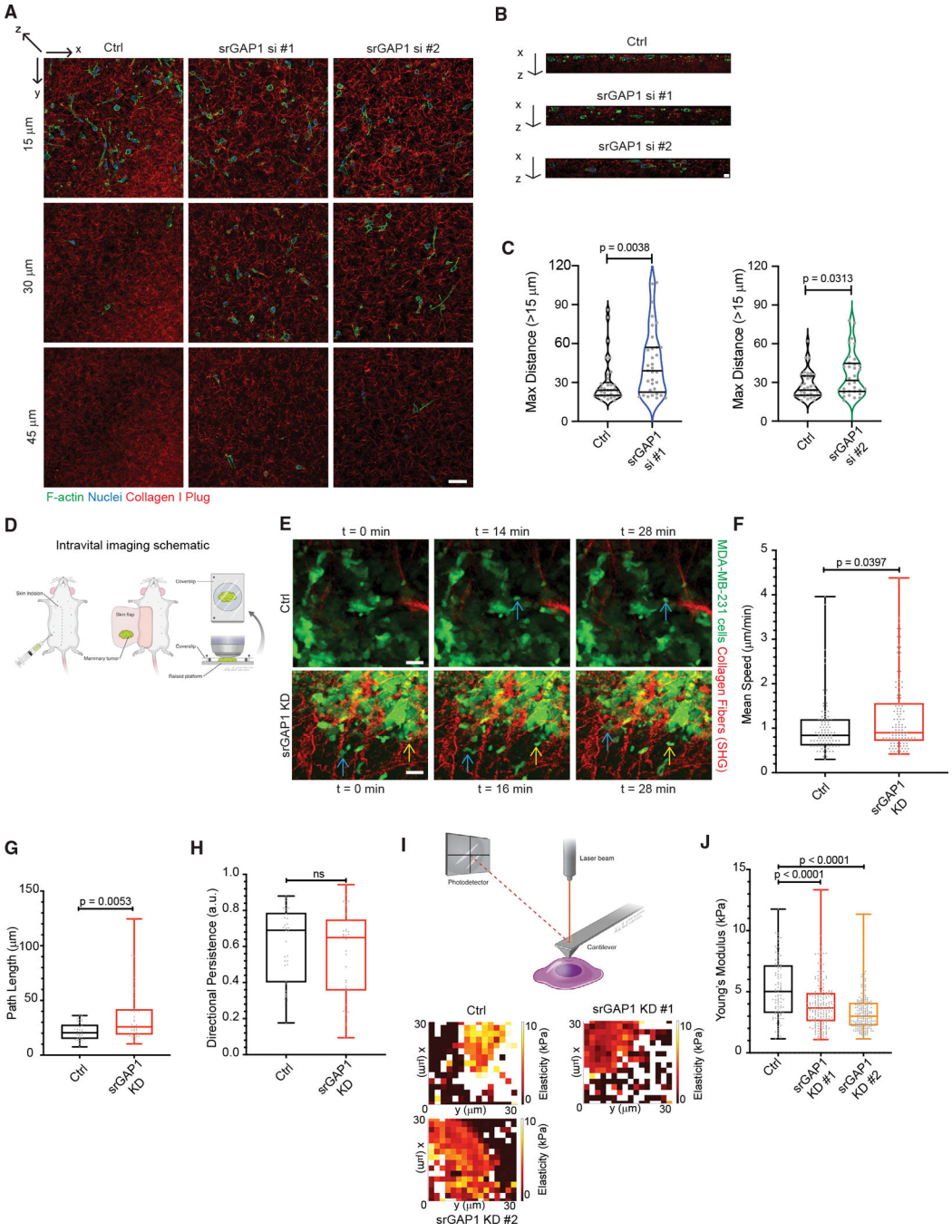

Figure 3. In vitro and *in vivo* invasion are regulated by srGAP1 expression

(A) Representative images of Ctrl, srGAP1 si #1, and srGAP1 si #2 MDA-MB-231 cells 3 days after being seeded on top of collagen I plugs. Images taken at 15, 30, and 45 µm in the z direction (deeper into collagen plug away from surface). Cells are labeled with phalloidin and DAPI, collagen I is fluorescently labeled. Scale bar, 50 µm.

(B) x-z images of representative collagen I plugs from (A). Scale bar, 10 µm.

(C) Maximum distance (>15 µm) Ctrl and srGAP1 si #1 cells (left) or Ctrl and srGAP1 si #2 MDA-MB-231 cells (right) invade into the collagen I plug. Each value is a single cell/field.

Left: n = 37 (Ctrl), 34 (srGAP1 si #1) cells. Right: n = 38 (Ctrl), 35 (srGAP1 si #2) cells. Data pooled over five independent experiments and represented as a violin plot; horizontal lines are median and interquartile range. Mann-Whitney U test, two-tailed.

(D) Schematic of intravital imaging setup.

(E) Three individual time frames from intravital imaging movies of Ctrl and srGAP1 KD #1 MDA-MB-231 primary tumors. Tumor cells in green, collagen fibers in red through second harmonic generation (SHG). Blue and yellow arrows indicate *in vivo* cell motility over time. One z slice shown at 0, 16, 28 min. Scale bar, 25 μm.

(F) Average mean speed of tumor cells moving in μm/min *in vivo* from (C). Data pooled from 3 Ctrl and 3 srGAP1 KD #1 mice, n = 94 (Ctrl) and 102 (srGAP1 KD #1) MDA-MB-231 tumor cells. Mann-Whitney U test, two-tailed. Data represented as a box and whisker plot, with median and interquartile range in the box and min and max as whiskers.

(G) Average path length of tumor cells that appear in a minimum of 10 frames of intravital imaging movies (t = 20–28 min). Data pooled from 3 Ctrl and 3 srGAP1 KD #1 mice, n = 27 (Ctrl) and 33 (srGAP1 KD #1) MDA-MB-231 tumor cells. Mann-Whitney U test, two-tailed. Data represented as a box and whisker plot, with median and interquartile range in the box and min and max as whiskers.

(H) Directional persistence of tumor cells that appear in a minimum of 10 frames of intravital imaging movies (t = 20–28 min). Data pooled from 3 Ctrl and 3 srGAP1 KD #1 mice, n = 27 (Ctrl) and 33 (srGAP1 KD #1) MDA-MB-231 tumor cells. Mann-Whitney U test, two-tailed. Data represented as a box and whisker plot, with median and interquartile range in the box and min and max as whiskers.

(I) Top: schematic of atomic force microscopy setup. Bottom: elasticity heatmaps of representative Ctrl, srGAP1 KD #1, and srGAP1 KD #2 MDA-MB-231 cells.

(J) Modulus of elasticity of Ctrl, srGAP1 KD #1, and srGAP1 KD #2 MDA-MB-231 cells using AFM. n = 100 (Ctrl), 200 (KD #1), and 200 (KD #2) measurements over 4, 8, and 8 cells, respectively. Mann-Whitney U test, two-tailed. Data represented as a box and whisker plot, with median and interquartile range in the box and min and max as whiskers.

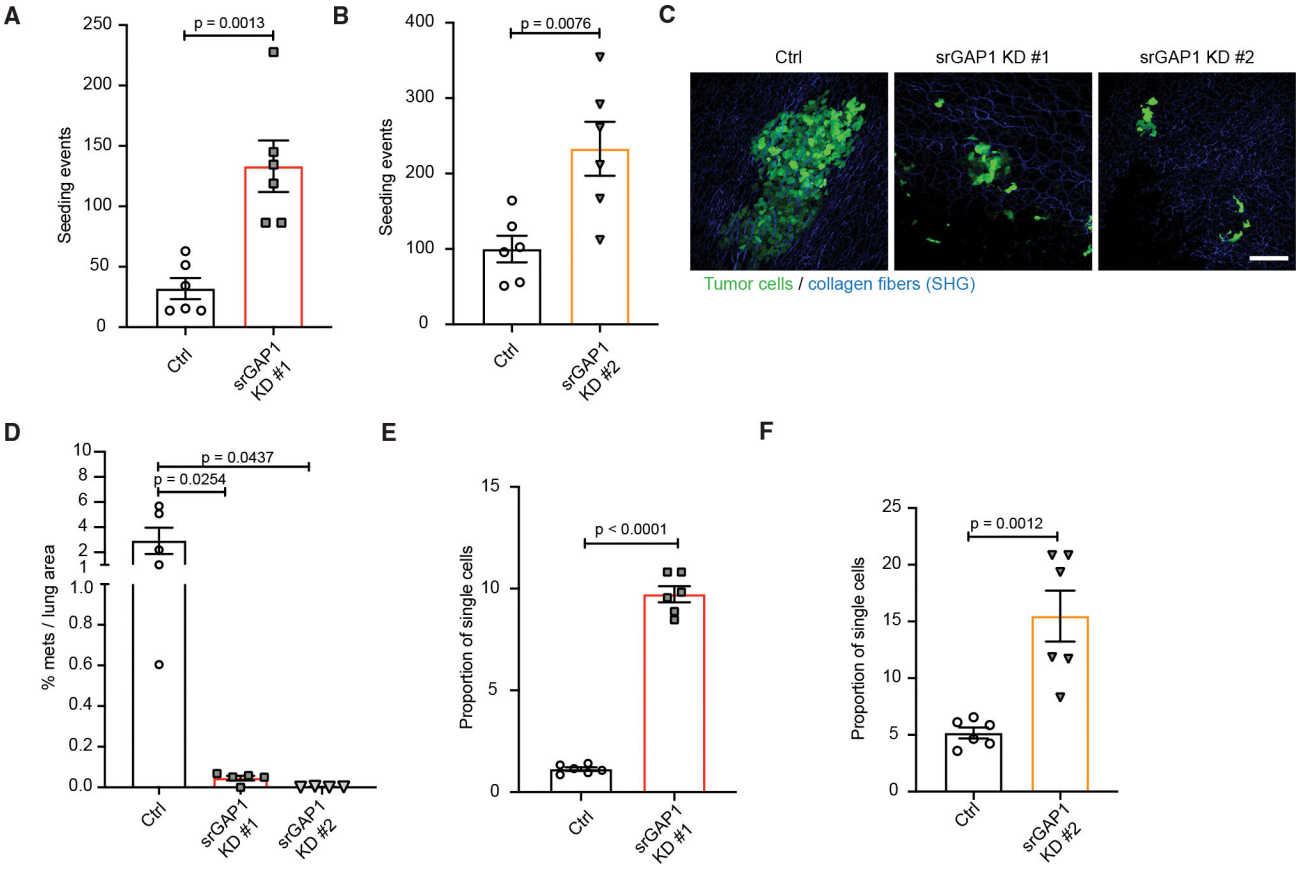

Figure 4. srGAP1^{low} cells are capable of seeding the lung but have reduced metastatic outgrowth

(A) Number of seeding events (single MDA-MB-231 tumor cells and clusters) relative to primary tumor mass (grams). Data pooled over two Ctrl and two srGAP1 KD #1 mice. Three 450 × 450 μm sections quantified per mouse. Unpaired t test, two-tailed, mean ± SEM.

(B) Number of seeding events (single MDA-MB-231 tumor cells and clusters) relative to primary tumor mass (grams). Data pooled over two Ctrl and two srGAP1 KD #2 mice. Three 450 × 450 μm sections quantified per mouse. Unpaired t test, two-tailed, mean ± SEM.

(C) Representative images of MDA-MB-231 lung metastasis in Ctrl, srGAP1 KD #1, and srGAP1 KD #2 mice. Maximum intensity z projection, tumor cells in green and collagen fibers in blue through second harmonic generation (SHG). Scale bar, 100 μm.

(D) Percent area of MDA-MB-231 metastasis per lung area measured (in mm^2). One H&E section measured per mouse, n = 5 (Ctrl), 5 (srGAP1 KD #1), and 4 (srGAP1 KD #2) mice. Unpaired t test, two-tailed, mean ± SEM.

(E) Quantification of the proportion of MDA-MB-231 single cells relative to mass of primary tumor per lung section. Data pooled over two Ctrl and two srGAP1 KD #1 mice. Three 450 × 450 μm sections quantified per mouse. Unpaired t test, two-tailed, mean ± SEM.

(F) Quantification of the proportion of MDA-MB-231 single cells relative to mass of primary tumor per lung section. Data pooled over two Ctrl and two srGAP1 KD #2 mice. Three 450 × 450 μm sections quantified per mouse. Unpaired t test, two-tailed, mean ± SEM.

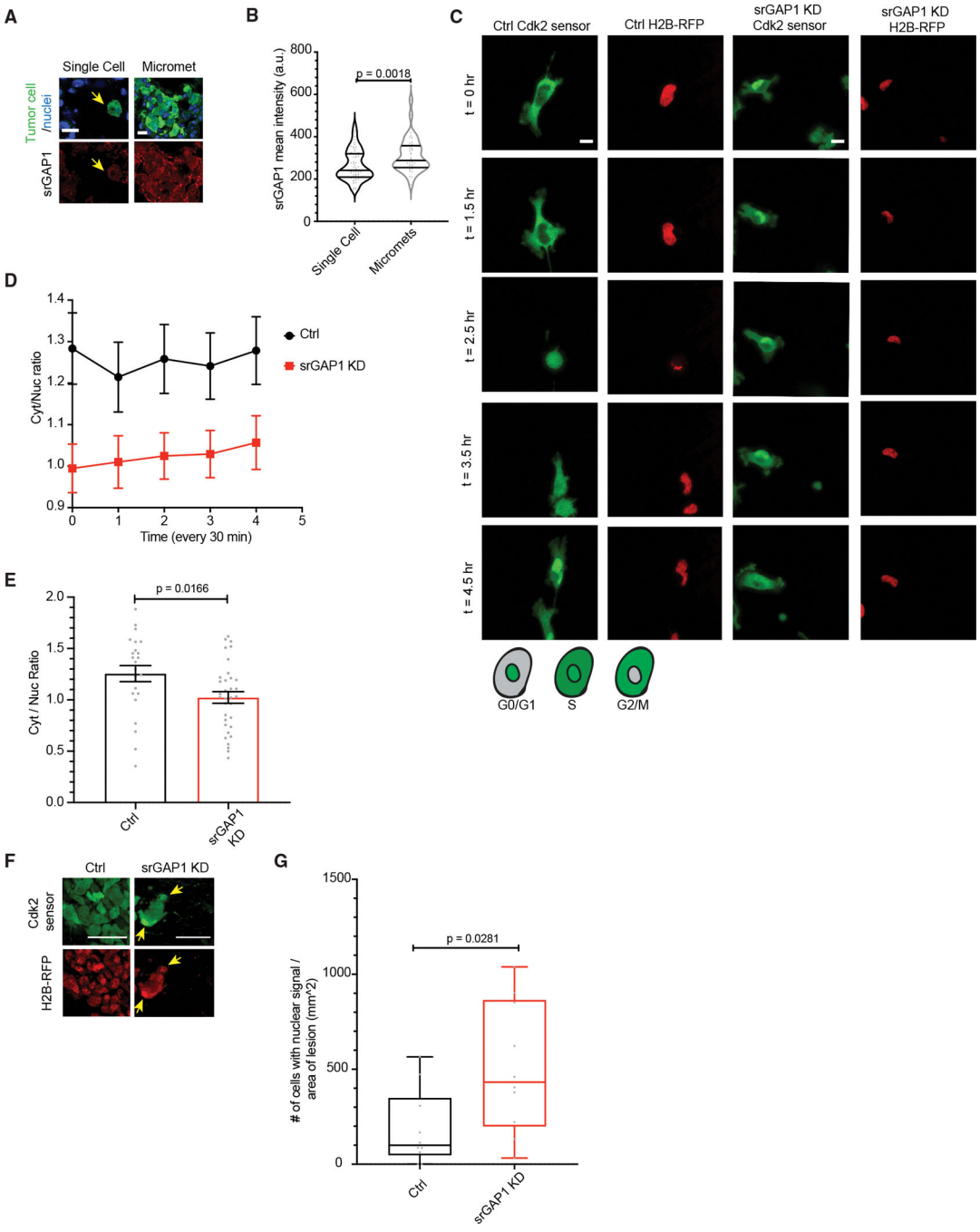

Figure 5. Solitary disseminated tumor cells have low srGAP1 expression

(A) Tissue staining of MDA-MB-231 single tumor cells and clusters in Ctrl mice lungs. Yellow arrow points to single cell. Top: GFP-labeled tumor cell, DAPI for nuclei. Bottom: srGAP1 staining. Scale bar, 10 μm.

(B) srGAP1 intensity of MDA-MB-231 tumor cells and clusters in Ctrl mice lung (mean intensity in a defined area calculated for individual tumor cells and clusters). Data pooled over two Ctrl mice, three 450 × 450 μm sections quantified per mouse. Mann Whitney U

test, two-tailed. Scale bar, 10 μm. Data represented as a violin plot; horizontal lines are median and interquartile range.

(C) Top: time-lapse imaging of MDA-MB-231 Ctrl and srGAP1 KD #1 cells expressing H2B-RFP and a DHB:Venus sensor for Cdk2 activity. Frames from live-cell imaging of cells plated on fibrillar collagen, time in hours. Scale bar, 10 μm. Bottom: schematic representing cells expressing DHB:Venus sensor: nuclear expression is G0/G1, nuclear and cytoplasmic expression is S, and cytoplasmic expression is G2/M.

(D) Quantification of cytoplasmic to nuclear (C/N) ratio of DHB:Venus sensor for Cdk2 activity over time for MDA-MB-231 Ctrl and srGAP1 KD #1 cells from (C). n = 24 (Ctrl), 34 (srGAP1 KD #1) cells, two independent experiments. C/N ratio calculated for five frames (2 h). Data represented as mean ± SEM.

(E) Average cytoplasmic to nuclear ratio of MDA-MB-231 Ctrl and KD #1 cells expressing the DHB:Venus sensor for Cdk2 activity and H2B-RFP. C/N calculated from live-cell imaging (averaged over 2 h) of cells plated on fibrillar collagen. n = 24 (Ctrl), 34 (srGAP1 KD #1) cells, two independent experiments. Unpaired t test, two-tailed.

(F) Images of lungs from Ctrl and srGAP1 KD #1 MDA-MB-231 xenografts expressing H2B-RFP and a DHB:Venus sensor for Cdk2 activity. Scale bars, 50 μm

(G) Number of MDA-MB-231 cells in the lung with nuclear DHB:Venus sensor expression relative to lesion area. Ten fields of view (255 × 255 μm) per mouse, data pooled over one Ctrl and one srGAP1 KD #1 mouse, each point is a field. Mann-Whitney U test, two-tailed. Data represented as a box and whisker plot, with median and interquartile range in the box and min and max as whiskers.

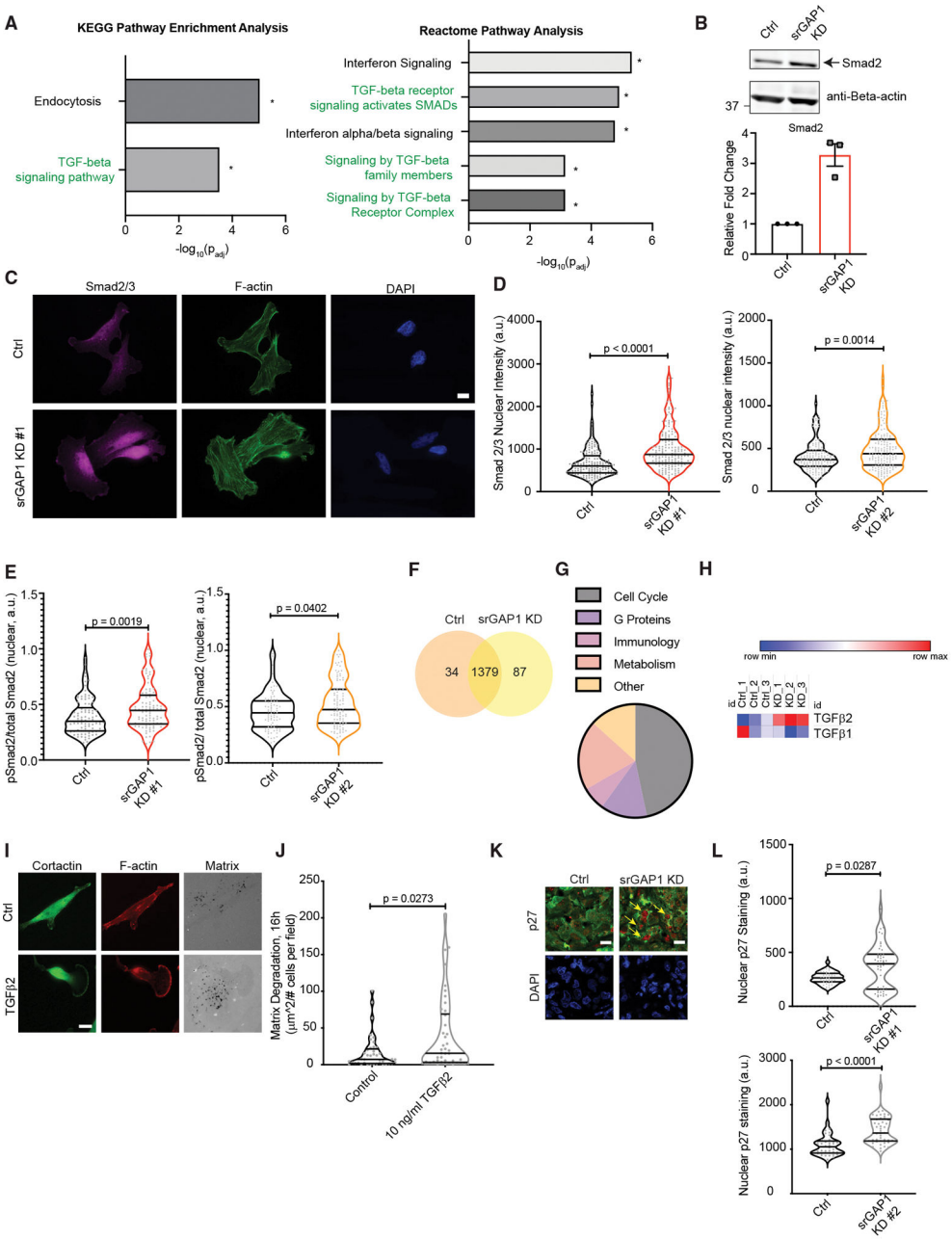

Figure 6. srGAP1^{low} cells have increased Smad2 activation and TGF-β2 secretion

(A) Left: KEGG pathway enrichment analysis; right: reactome pathway analysis of differentially expressed genes in srGAP1 KD #1 MDA-MB-231 tumors in relation to Ctrl tumors, *$p_{adj} < 0.05$.

(B) Top: immunoblot of Smad2 in Ctrl and srGAP1 KD #1 MDA-MB-231 cells using an anti-Smad2/3 antibody. Loading control, anti-β-actin. Bottom: densitometry analysis of Smad2 protein levels in Ctrl and KD #1 cells, three biological replicates.

(C) Immunofluorescence of Smad2/3 in Ctrl and srGAP1 KD #1 MDA-MB-231 cells. Left: Smad2/3. Middle: phalloidin staining for F-actin. Right: DAPI for nuclear staining. Scale bar, 10 μm.
(D) Smad2/3 nuclear intensity per cell. Left: n = 170 (Ctrl), 171 (srGAP1 KD #1) MDA-MB-231 cells. Right: n = 151 (Ctrl) cells, n = 169 (srGAP1 KD #2) MDA-MB-231 cells. Data over three independent experiments, Mann-Whitney U test, two-tailed. Data represented as a violin plot; horizontal lines are median and interquartile range.
(E) pSmad2/total Smad2 nuclear intensity ratio. Left: n = 90 (Ctrl), 94 (srGAP1 KD #1) MDA-MB-231 cells. Right: n = 80 (Ctrl), 99 (srGAP1 KD #2) MDA-MB-231 cells. Data over three independent experiments, Mann-Whitney U test, two-tailed. Data represented as a violin plot; horizontal lines are median and interquartile range.
(F) Differential expression of proteins from secretome analysis of conditioned medium from srGAP1 KD #1 MDA-MB-231 cells in relation to conditioned medium from Ctrl cells. Data visualized as a Venn diagram, three biological replicates and two technical duplicates.
(G) Pathway enrichment analysis of secretome (proteomics of conditioned medium) from srGAP1 KD #1 MDA-MB-231 cells in relation to conditioned medium from Ctrl cells.
(H) Expression of TGF-β ligands from proteomics data comparing conditioned medium from Ctrl and srGAP1 KD #1 MDA-MB-231 cells. Each data point is a biological replicate (averaged technical duplicates).
(I) Matrix degradation of MDA-MB-231 Ctrl cells plated on gelatin and stimulated with 10 ng/mL TGF-β2, 16 h. Left: cortactin. Middle: phalloidin stain for F-actin. Right: fluorescent gelatin matrix. Scale bar, 10 μm.
(J) Matrix degradation of MDA-MB-231 Ctrl cells stimulated with 10 ng/mL TGF-β2 plated on gelatin, 16 h. Data from three independent experiments and represented as a violin plot, horizontal lines are median and interquartile range. n = 41 (Ctrl), 42 (TGF-β2-stimulated) fields quantified. Mann-Whitney U test, two-tailed.
(K) Nuclear p27 staining intensity of MDA-MB-231 Ctrl and srGAP1 KD #2 primary tumors. Top: p27. Bottom: DAPI for nuclei. Scale bar, 10 μm.
(L) Nuclear p27 staining intensity of MDA-MB-231 primary tumors. Top: data pooled over two Ctrl and two srGAP1 KD #1 mice. n = 39 (Ctrl) cells, n = 48 (srGAP1 KD #1) cells. Two 246 × 246 μm sections quantified per mouse. Mann-Whitney U test, two-tailed. Bottom: data pooled over two Ctrl and two srGAP1 KD #2 mice. One 388 × 388 μm section quantified per mouse. n = 38 (Ctrl) cells, n = 46 (srGAP1 KD #2) cells. Mann-Whitney U test, two-tailed. Data represented as a violin plot; horizontal lines are median and interquartile range.

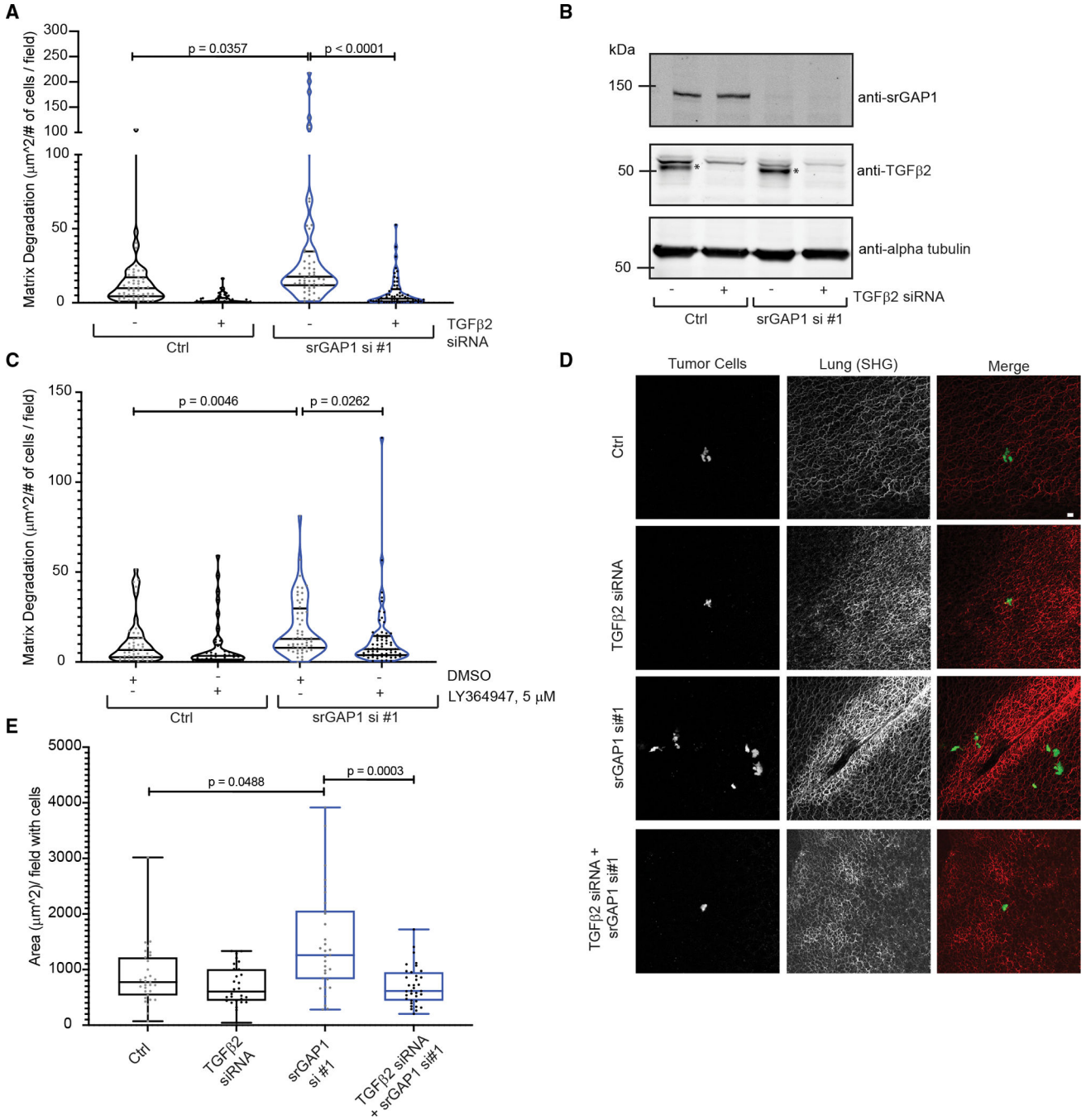

Figure 7. TGF-β2-mediated signaling regulates srGAP1^{low} phenotypes

(A) Matrix degradation of Ctrl and srGAP1 si #1 MDA-MB-231 cells with or without depletion of TGF-β2 by siRNA. Cells plated on fluorescent gelatin for 16 h. n = 51 (Ctrl), 47 (Ctrl + TGF-β2 siRNA), 52 (srGAP1 si #1), and 58 (srGAP1 si #1 + TGF-β2 siRNA) fields quantified. Data are from three independent experiments and represented as a violin plot, horizontal lines are median and interquartile range. Kruskal-Wallis test, corrected with Dunn's test.

(B) Immunoblot of Ctrl and srGAP1 si #1 MDA-MB-231 cells with or without depletion of TGF-β2 by siRNA. Top blot: anti-srGAP1. Middle blot: anti-TGF-β2, * represents the TGF-β2 band. Bottom blot: loading control: anti-α-tubulin.

(C) Matrix degradation of Ctrl and srGAP1 si #1 MDA-MB-231 cells with DMSO or 5 μM LY364947. Cells treated in serum-free medium with DMSO or 5 μM LY364947 for 24 h, then plated on fluorescent gelatin for 16 h with DMSO or 5 μM LY364947. n = 45 (Ctrl + DMSO), 38 (Ctrl +5 μM LY364947), 52 (srGAP1 si #1 + DMSO), and 61 (srGAP1 si #1 + 5 μM LY364947) fields quantified. Data are from three independent experiments and represented as a violin plot, horizontal lines are median and interquartile range. Kruskal-Wallis test, corrected with Dunn's test.

(D) Representative images of cells seeding the lung after tail-vein injections. Left panel: GFP-labeled MDA-MB-231 tumor cells. Middle panel: fibrillar collagen (second harmonic generation). Right panel: merge, tumor cells in green and fibrillar collagen in red. Scale bar, 20 μm.

(E) Area of tumor cells that have extravasated into the lung per field containing cells. GFP-labeled MDA-MB-231 Ctrl and srGAP1 si #1 MDA-MB-231 cells with or without depletion of TGF-β2 by siRNA. Cells injected into the tail-vein of mice. n = 31 (Ctrl), 31 (Ctrl + TGF-β2 siRNA), 29 (srGAP1 si #1), and 25 (srGAP1 si #1 + TGF-β2 siRNA) fields quantified, pooled over 5, 5, 4, and 5 mice, respectively. Data are represented as a box and whisker plot; horizontal lines are median and interquartile range. Kruskal-Wallis test, corrected with Dunnett T3 test.

KEY RESOURCES TABLE

REAGENT or RESOURCE	SOURCE	IDENTIFIER
Antibodies		
Rabbit anti-srGAP1	Bethyl Labs	A301-286A; RRID:AB_938002
Rabbit anti-srGAP2	Abcam	ab124958; RRID:AB_10971187
Rabbit anti-Smad2/3	CST	8685T
Mouse anti-alpha-tubulin	Sigma	T6074; RRID:AB_477582
Rabbit anti-Beta-actin	Abcam	ab8227; RRID:AB_2305186
Rabbit anti-TGFβ2	Abclonal	A3640; RRID:AB_2765199
Rabbit anti-srGAP1	Proteintech	13252-1-AP; RRID:AB_2270916
Rabbit anti-Cortactin	Abcam	ab81208; RRID:AB_1640383
Mouse anti-Tks5	Millipore	MABT336
Mouse anti-Cortactin	Millipore	05-180-I
Rabbit anti-pSmad2	CST	3108S
Mouse anti-Smad2	LSBio	LS-C169392
Chicken anti-GFP	Aves Labs	GFP-1010; RRID:AB_2307313
Goat anti-p27	LSBio	LS-B3943; RRID:AB_10700493
Rabbit anti-p27	CST	3686S; RRID:AB_2077850
Bacterial and virus strains		
Subcloning Efficiency™ DH5α Competent Cells	Thermo Fisher	18265017
Chemicals, peptides, and recombinant proteins		
Recombinant Human TGF-beta 2/TGFP2 Protein	AbClonal	RP00452
LY364947	Selleck Chemical	S2805
Rat-tail Collagen I	Corning	354236
Hoechst 33342	BD Pharmingen	561908
Gelatin from Pig Skin, Oregon Green™ 488 Conjugate	Fisher Scientific	G13186
Gelatin solution	Sigma-Aldrich	G1393
Critical commercial assays		
FITC Annexin V Apoptosis Detection Kit with 7-AAD	BioLegend	640922
Deposited data		
RNAseq	Repository	GEO (GSE210488)
Proteomics	Repository	PRIDE (PXD026102)
Experimental models: Cell lines		
MDA-MB-231	ATCC	HTB-26
BT549	ATCC	HTB-122
HS578T	ATCC	HTB-126

REAGENT or RESOURCE	SOURCE	IDENTIFIER
MCF7	ATCC	HTB-22
T47D	ATCC	CRL-2865
HEK 293 T/17	ATCC	CRL-11268
Experimental models: Organisms/strains		
NCG mice (NOD-*Prkdc*^{em26Cd52}*Il2rg*^{em26Cd22}/NjuCrl)	Charles River Lab	Strain Code: 572
nu/nu mice (Crl:NU-*Foxn1*^{nu})	Charles River Lab	Strain Code: 490
Zebrafish (*Danio rerio*, tg(*kdrl:RFP*))	Benjamin Martin	
Oligonucleotides		
Human srGAP1 siRNA #1 (5'-GCAGAUAAGUGAGGAUUCU-3')	IDT	This paper
Human srGAP1 siRNA #2 ('5-CAUGAGGGCUUAGACAUUA 3')	IDT	This paper
Human TGFβ2 siRNA	Thermo Fisher	s14061
Non-targeting Control siRNA against luciferase (5'-CGTACGCGGAATACTTCGA-3')	IDT	(Juin et al., 2014)
Recombinant DNA		
pHIV-H2B-mRFP	Addgene	18982
FG12-GFP	Marisol Soengas	(Olmeda et al., 2017)
CSII-EF-DHB-Venus	Sabrina Spencer	(Spencer et al., 2013)
pLifeact-mRuby	Violaine Moreau	(Juin et al., 2014)
CFP-YFP RhoA biosensor	Louis Hodgson	(Pertz et al., 2006)
CFP-YFP Cdc42 biosensor	Louis Hodgson	(Hanna et al., 2014)
CFP-YFP Rac1 biosensor	Louis Hodgson	(Miskolci et al., 2016)
plKO.1 shRNA human srGAP1 #1	AECOM	RHS3979-9614755
pLKO.1 shRNA human srGAP1 #2	AECOM	RHS3979-98492192
pLKO.1 Lentiviral Non-targeting Control shRNA	Horizon	RHS6848
Software and algorithms		
Graphpad Prism 9	https://www.graphpad.com/	N/A
Scaffold 5	https://www.proteomesoftware.com	N/A
FIJI	https://imagej.net/software/fiji/	N/A
Imaris	Oxford Instruments	N/A